Enhancing Certified Robustness via Block Reflector Orthogonal Layers and Logit Annealing Loss

Bo-Han Lai [*] **Pin-Han Huang** [*] **Bo-Han Kung** [*] **Shang-Tse Chen** [1]

Abstract

Lipschitz neural networks are well-known for providing certified robustness in deep learning. In this paper, we present a novel, efficient Block Reflector Orthogonal (BRO) layer that enhances the capability of orthogonal layers on constructing more expressive Lipschitz neural architectures. In addition, by theoretically analyzing the nature of Lipschitz neural networks, we introduce a new loss function that employs an annealing mechanism to increase margin for most data points. This enables Lipschitz models to provide better certified robustness. By employing our BRO layer and loss function, we design BRONet — a simple yet effective Lipschitz neural network that achieves state-of-the-art certified robustness. Extensive experiments and empirical analysis on CIFAR-10/100, Tiny-ImageNet, and ImageNet validate that our method outperforms existing baselines. The implementation is available at GitHub Link.

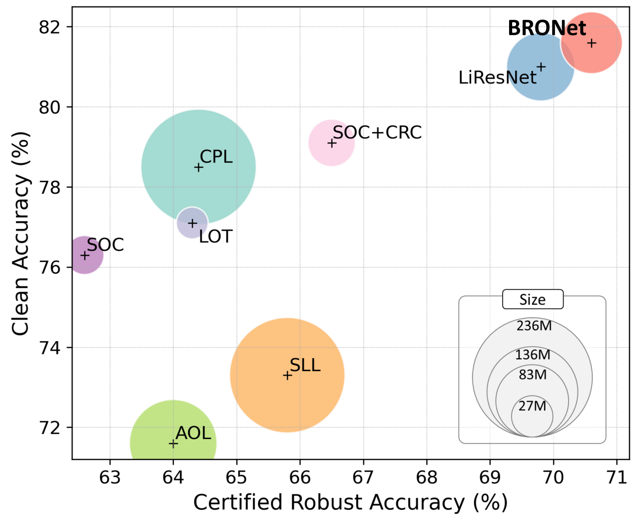

Figure 1. Visualization of model performance on CIFAR-10. The circle size denotes model size.

1. Introduction

Although deep learning has been widely adopted in various fields (Wang et al., 2022; Brown et al., 2020), it is shown to be vulnerable to adversarial attacks (Szegedy et al., 2014). This kind of attack crafts an imperceptible perturbation on images (Goodfellow et al., 2014) or voices (Carlini & Wagner, 2018) to make AI systems make incorrect predictions. In light of this, many adversarial defense methods have been proposed to improve the robustness, which can be categorized into empirical defenses and certified defenses. Common empirical defenses include adversarial training (Madry et al., 2018; Shafahi et al., 2019; Wang et al., 2023) and preprocessing-based methods (Samangouei et al., 2018; Das et al., 2018; Lee & Kim, 2023). Although often effective in practice, these approaches cannot provide robustness guarantees and may fail against more sophisticated attacks. Certified defenses, unlike empirical ones, provide provable robustness by ensuring no adversarial examples exist within an ℓ_p-norm ball of radius ε centered on the prediction point.

Certified defenses against adversarial attacks are broadly categorized into *probabilistic* and *deterministic* (Li et al., 2023) methods. Randomized smoothing (Cohen et al., 2019; Lecuyer et al., 2019; Yang et al., 2020) is a prominent probabilistic approach, known for its scalability in providing certified robustness. However, its reliance on extensive sampling substantially increases computational overhead during inference, limiting its practical deployment. Furthermore, the certification provided is probabilistic in nature.

Conversely, deterministic methods, exemplified by interval bound propagation (Ehlers, 2017; Gowal et al., 2018; Mueller et al., 2023; Shi et al., 2022) and CROWN (Wang et al., 2021; Zhang et al., 2022), efficiently provide deterministic certification. These methods aim to approximate the lower bound of worst-case robust accuracy to ensure deterministic robustness guarantees. Among various deterministic methods, neural networks with Lipschitz con-

[*]Equal contribution [1]Department of Computer Science and Information Engineering, National Taiwan University, Taiwan. Correspondence to: Shang-Tse Chen <stchen@csie.ntu.edu.tw>.

Proceedings of the 42^{nd} International Conference on Machine Learning, Vancouver, Canada. PMLR 267, 2025.

straints are able to compute the lower bound of worst-case robust accuracy with a single forward pass, making them the most time-efficient at inference time. They are known as Lipschitz neural networks.

Lipschitz neural networks are designed to ensure that the entire network remains Lipschitz-bounded. This constraint limits the sensitivity of the outputs to input perturbations, thus providing certifiable robustness by controlling changes in the logits. A promising approach to constructing Lipschitz networks focuses on designing orthogonal layers, which inherently satisfy the 1-Lipschitz constraint. Furthermore, these layers help mitigate the issue of vanishing gradients due to their norm-preserving properties. Nonetheless, existing methods for constructing orthogonal layers remain computationally expensive, thus hindering their integration into more sophisticated neural architectures.

In this work, we introduce the **Block Reflector Orthogonal (BRO)** layer, which outperforms state-of-the-art orthogonal layers in terms of computational efficiency as well as robust and clean accuracy. We utilize it to develop various Lipschitz neural networks, underscoring its utility across architectures. Building upon the BRO layer, we introduce **BRONet**, a new Lipschitz neural network exhibiting promising results.

Moreover, we delve into Lipschitz neural networks, analyzing their inherent limited capability. Building on this analysis, we introduce a novel loss function, the *Logit Annealing* loss, which is empirically shown to be highly effective for training Lipschitz neural networks. The certification results of the proposed method outperform state-of-the-art methods with reasonable number of parameters, as Figure 1 shows.

Our contributions are summarized as follows:

- We propose a novel BRO method to construct orthogonal layers using low-rank parameterization. It is both time and memory efficient, while also being stable during training by eliminating the need for iterative approximation algorithms.
- The proposed BRO Layer improves certified robustness while reducing the resource demands of orthogonal layers, thereby expanding their applicability to more advanced architectures.
- We construct various Lipschitz networks using the BRO method, including newly designed BRONet, which achieves state-of-the-art certified robustness.
- Based on our theoretical analysis, we develop a novel loss function, the Logit Annealing loss, which is effective for training Lipschitz neural networks via an annealing mechanism.
- Through extensive experiments, we demonstrate the effectiveness of our proposed method on the CIFAR-10/100, Tiny-ImageNet, and ImageNet datasets.

2. Preliminaries

2.1. Certified Robustness with Lipschitz Networks

Consider a function $f : \mathbb{R}^m \to \mathbb{R}^n$. The function is said to exhibit L-Lipschitz continuity under the ℓ_2-norm if there exists a non-negative constant L such that:

$$L = \operatorname{Lip}(f) = \sup_{x_1, x_2 \in \mathbb{R}^m} \frac{\|f(x_1) - f(x_2)\|}{\|x_1 - x_2\|}, \quad (1)$$

where $\|\cdot\|$ represents the ℓ_2 norm. This relationship indicates that any variation in the network's output, measured by the norm, is limited to at most L times the corresponding variation in its input. This property effectively characterizes the network's stability and sensitivity to input changes. Specifically, under the ℓ_2-norm, the Lipschitz constant is equivalent to the spectral norm of the function's Jacobian matrix.

Assuming $f(x)$ are the output logits of a neural network, and t denotes the target label. We say $f(x)$ is certifiably robust with a certified radius ε if $\arg\max_i f(x+\delta)_i = t$ for all perturbations $\{\delta : \|\delta\| \leq \varepsilon\}$. Determining the certified radii is crucial for certifiable robustness and presents a significant challenge. However, in L-Lipschitz neural networks, ε can be easily calculated using $\varepsilon = \max(0,\ \mathcal{M}_f(x)/\sqrt{2}L)$, where $\mathcal{M}_f(x)$ denotes the logit difference between the ground-truth class and the runner-up class in the network output. That is, $\mathcal{M}_f(x) = f(x)_t - \max_{k \neq t} f(x)_k$ (Tsuzuku et al., 2018; Li et al., 2019).

2.2. Lipschitz Constant Control & Orthogonality

Obtaining the exact Lipschitz constant for general neural networks is known to be an NP-hard problem (Virmaux & Scaman, 2018). However, there are efficient methods available for computing it on a layer-by-layer basis. Once the Lipschitz constant for each layer is determined, the Lipschitz composition property allows for the calculation of the overall Lipschitz constant for the entire neural network. The Lipschitz composition property states that given two functions f and g with Lipschitz constants L_f and L_g, their composition $h = g \circ f$ is also Lipschitz with a constant $L_h \leq L_g \cdot L_f$. We can use this property to upper-bound the Lipschitz constant of a complex neural network f:

$$f = \phi_l \circ \phi_{l-1} \circ \ldots \circ \phi_1, \quad \operatorname{Lip}(f) \leq \prod_{i=1}^{l} \operatorname{Lip}(\phi_i). \quad (2)$$

Thus, if the Lipschitz constant of each layer is properly regulated, robust certification can be provided. A key relevant property is orthogonality, characterized by the isometry property $\|Wx\| = \|x\|$ for a given operator W. Encouraging orthogonality is crucial for controlling the Lipschitz constant while preserving model expressiveness (Anil et al., 2019), as it avoids gradient vanishing. An illustrative example is the replacement of common element-wise activations, such as ReLU, with MaxMin (Anil et al., 2019; Chernodub & Nowicki, 2016) in the Lipschitz network literature. While both are 1-Lipschitz, MaxMin demonstrates superior empirical performance for being gradient-norm preserving.

3. Related Work

Orthogonal Layers Orthogonality in neural networks is crucial for various applications, including certified robustness via Lipschitz-based methods, GAN stability (Müller et al., 2019), and training very deep networks with inherent gradient preservation (Xiao et al., 2018). While some approaches implicitly encourage orthogonality through regularization or initialization (Qi et al., 2020; Xiao et al., 2018), explicit methods for constructing orthogonal layers have garnered significant attention, as evidenced by several focused studies in this area. Li et al. (2019) proposed *Block Convolution Orthogonal Parameterization (BCOP)*, which utilizes an iterative algorithm for orthogonalizing the linear transformation within a convolution. Trockman & Kolter (2021) introduced a method employing the *Cayley transformation* $W = (I - V)(I + V)^{-1}$, where V is a skew-symmetric matrix. Similarly, Singla & Feizi (2021b) developed the *Skew-Orthogonal Convolution (SOC)*, employing an exponential convolution mechanism for feature extraction. Additionally, Xu et al. (2022) proposed the *Layer-wise Orthogonal training (LOT)*, an analytical solution to the orthogonal Procrustes problem (Schönemann, 1966), formulated as $W = (VV^T)^{-1/2}V$. This approach requires the Newton method to approximate the internal matrix square root. Yu et al. (2022) proposed the *Explicitly Constructed Orthogonal Convolution (ECO)* to enforce all singular values of the convolution layer's Jacobian to be one.

Notably, SOC and LOT achieve state-of-the-art certified robustness for orthogonal layers. Most matrix reparameterization-based methods can be easily applied for dense layers, such as Cayley, SOC, and LOT. A recently proposed orthogonalization method for dense layers is *Cholesky* (Hu et al., 2024), which explicitly performs QR decomposition on the weight matrix via Cholesky decomposition.

Other 1-Lipschitz Layers A relaxation of isometry constraints, namely, $\|Wx\| \leq \|x\|$, facilitates the development of extensions to orthogonal layers, which are 1-Lipschitz layers. Prach & Lampert (2022) introduced the *Almost Orthogonal Layer (AOL)*, which is a rescaling-based parameterization method. Meanwhile, Meunier et al. (2022) proposed the *Convex Potential Layer (CPL)*, leveraging convex potential flows to construct 1-Lipschitz layers. Building on CPL, Araujo et al. (2023) presented *SDP-based Lipschitz Layers (SLL)*, incorporating AOL constraints for norm control. Most recently, Wang & Manchester (2023) introduced the Sandwich layer, a direct parameterization that analytically satisfies the semidefinite programming conditions outlined by Fazlyab et al. (2019).

Lipschitz Regularization While the aforementioned methods control Lipschitz constant by formulating constrained layers with guaranteed Lipschitz bound, Lipschitz regularization methods estimate the layer-wise Lipschitz constant via power iteration (Farnia et al., 2019) and apply regularization to control it. Leino et al. (2021) employed a Lipschitz regularization term to maximize the margin between the ground truth and runner-up class in the loss function. Hu et al. (2023; 2024) further proposed a new Lipschitz regularization method *Efficiently Margin Maximization (EMMA)*, which dynamically adjust all the non-ground-truth logits before calculating the cross-entropy loss.

4. BRO: Block Reflector Orthogonal Layer

In this section, we introduce the BRO layer, designed to provide certified robustness via low-rank orthogonal parameterization. First, we detail the fundamental properties of our method. Next, we leverage the 2D-convolution theorem to develop the BRO convolutional layer. Finally, we conduct a comparative analysis of our BRO with existing state-of-the-art orthogonal layers.

4.1. Low-rank Orthogonal Parameterization Scheme

The core premise of BRO revolves around a low-rank orthogonal parameterization, as introduced by the following proposition. A detailed proof is provided in Appendix A.1.

Proposition 1. *Let $V \in \mathbb{R}^{m \times n}$ be a matrix of rank n, and, without loss of generality, assume $m \geq n$. Then the parameterization $W = I - 2V(V^TV)^{-1}V^T$ satisfies the following properties:*

1. *W is orthogonal and symmetric, i.e., $W^T = W$ and $W^TW = I$.*
2. *W is an n-rank perturbation of the identity matrix, i.e., it has n eigenvalues equal to -1 and $m-n$ eigenvalues equal to 1.*
3. *W degenerates to the negative identity matrix when V is a full-rank square matrix.*

This parameterization draws inspiration from the block reflector (Dietrich, 1976; Schreiber & Parlett, 1988), which is widely used in parallel QR decomposition and is also important in other contemporary matrix factorization techniques. This approach enables the parameterization of an orthogonal matrix derived from a low-rank unconstrained matrix, thereby improving computational efficiency.

Building on the definitive property of the proposition above, we initialize the parameter matrix V as non-square to prevent it from degenerating into a negative identity matrix.

While the above discussion focuses on weight matrices for dense layers, the same parameterization can also be applied to construct orthogonal convolution operations, as both are linear transformations. However, a significant difference arises because the BRO formulation requires an inverse convolution computation, which is difficult to solve in the spatial domain. This leads us to address the issue in the Fourier domain. Furthermore, it is essential to note that directly orthogonalizing each convolution kernel does not result in an orthogonal convolution (Achour et al., 2022).

To introduce the BRO convolution, we begin by defining the process given an unconstrained kernel $V \in \mathbb{R}^{c\times n\times k\times k}$, where each slicing $V_{:,:,i,j}$ is defined as in Proposition 1. Define FFT : $\mathbb{R}^{s\times s} \to \mathbb{C}^{s\times s}$ as the 2D Fourier transform operator and $\text{FFT}^{-1} : \mathbb{C}^{s\times s} \to \mathbb{C}^{s\times s}$ as its inverse, where $s \times s$ denotes the spatial dimensions, and the input will be zero-padded to $s \times s$ if the original shape is smaller. The 2D convolution theorem (Jain, 1989) asserts that the circular convolution of two matrices in the spatial domain corresponds to their element-wise multiplication in the Fourier domain. Extending this idea, Trockman & Kolter (2021) demonstrates that multi-channel 2D circular convolution in the Fourier domain corresponds to performing a batch of matrix-vector products. By orthogonalizing each of these matrices, the convolution operation becomes orthogonal. Leveraging this insight, we can perform orthogonal convolution as follows.

Let $\tilde{X} = \text{FFT}(X)$ and $\tilde{V} = \text{FFT}(V)$, the convolution output Y is then computed as $Y = \text{FFT}^{-1}(\tilde{Y})$ and $\tilde{Y}_{:,i,j} = \tilde{W}_{:,:,i,j}\tilde{X}_{:,i,j}$, where $\tilde{W}_{:,:,i,j} = I - 2\tilde{V}_{:,:,i,j}(\tilde{V}^*_{:,:,i,j}\tilde{V}_{:,:,i,j})^{-1}\tilde{V}^*_{:,:,i,j}$ and i, j are the pixel indices. Note that the FFT is performed on the spatial (pixel) dimensions, while the orthogonal multiplication is applied on the channel dimension.

Proposition 2. *Let $\tilde{X} = FFT(X) \in \mathbb{C}^{c\times s\times s}$ and $\tilde{V} = FFT(V) \in \mathbb{C}^{c\times n\times s\times s}$, the proposed BRO convolution $Y = FFT^{-1}(\tilde{Y})$, where $\tilde{Y}_{:,i,j} = \tilde{W}_{:,:,i,j}\tilde{X}_{:,i,j}$ and $\tilde{W}_{:,:,i,j} = I - 2\tilde{V}_{:,:,i,j}(\tilde{V}^*_{:,:,i,j}\tilde{V}_{:,:,i,j})^{-1}\tilde{V}^*_{:,:,i,j}$, is a real,* orthogonal *multi-channel 2D circular convolution.*

Importantly, the BRO convolution is a 2D circular convolution that is orthogonal, as demonstrated by Proposition 2. Furthermore, although the BRO convolution primarily involves complex number computations in the Fourier domain, the output Y remains real. The detailed proof of Proposition 2 is provided in Appendix A.2.

Algorithm 1 details the proposed method, illustrating the case where the input and output channels are equal to c. Following Xu et al. (2022), we zero pad the input and parameters to size $s + 2k'$, where $2k'$ is the extra padding to alleviate the circular convolution effect across edges. A discussion on the implementation of zero-padding, along with an observation of a minor norm drop resulting from the removal of output padding, is provided in Appendix A.4. For layers where the input dimension differs from the output dimension, we enforce the 1-Lipschitz constraint via semi-orthogonal matrices. For details about the semi-orthogonal layers, please refer to Appendix A.3.

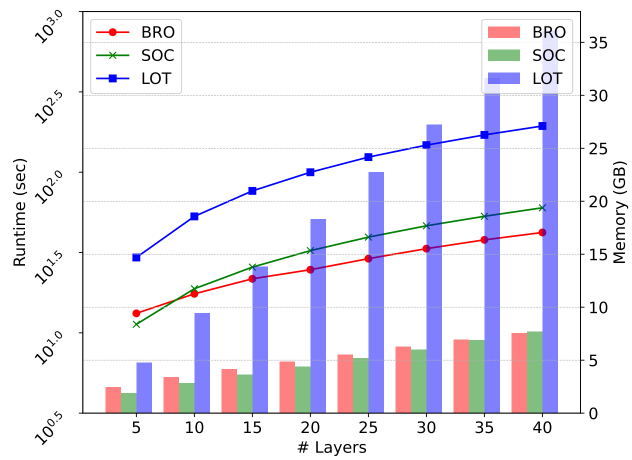

Figure 2. Comparison of runtime and memory usage among SOC, LOT, and the proposed BRO.

4.2. Properties of BRO Layer

This section compares BRO to SOC and LOT, the state-of-the-art orthogonal layers.

Iterative Approximation-Free Both LOT and SOC utilize iterative algorithms for constructing orthogonal convolution layers. Although these methods' error bounds are theoretically proven to converge to zero, empirical observations suggest potential violations of the 1-Lipschitz constraint. Prior work (Béthune et al., 2022) has noted that SOC's construction may result in non-1-Lipschitz layers due to approximation errors inherent in the iterative process involving a finite number of terms in the Taylor expansion. Regarding LOT, we observe numerical instability during training due to the Newton method for orthogonal matrix computation. Specifically, the Newton method breaks the orthogonality when encountering ill-conditioned parameters, even with the 64-bit precision computation recommended by the authors. An illustrative example is that using Kaiming initialization (He et al., 2015) instead of identity initialization results in a non-orthogonal layer. Detailed experiments are provided in Appendix D.7. In contrast, the proposed BRO constructs orthogonal layers without iterative approximation, ensuring both orthogonality and robustness certification validity.

Time and Memory Efficiency LOT's internal Newton method requires numerous steps to approximate the square

Algorithm 1 BRO Convolution Layer

Input: Tensor $X \in \mathbb{R}^{c\times s\times s}$, Kernel $V \in \mathbb{R}^{c\times n\times k\times k}$ with $n \leq c$, $k' = \lfloor k/2 \rfloor$. ▷ c is channel size.
Output: Tensor $Y \in \mathbb{R}^{c_{out}\times w\times w}$, the orthogonal convolution applied to X parameterized by V.
$X^{\text{pad}} :=$ zero_pad$(X, (k', k', k', k')) \in \mathbb{R}^{c\times(s+2k')\times(s+2k')}$
$V^{\text{pad}} :=$ zero_pad$(V, (0, 0, s + 2k' - k, s + 2k' - k)) \in \mathbb{R}^{c\times n\times(s+2k')\times(s+2k')}$
$\tilde{X} := \mathrm{FFT}(X^{\text{pad}}) \in \mathbb{C}^{c\times(s+2k')\times(s+2k')}$
$\tilde{V} := \mathrm{FFT}(V^{\text{pad}}) \in \mathbb{C}^{c\times n\times(s+2k')\times(s+2k')}$
for all $i, j \in \{1, \ldots, s + 2k'\}$ **do**
  $\tilde{Y}_{:,i,j} := (I - 2\tilde{V}_{:,:,i,j}(\tilde{V}^*_{:,:,i,j}\tilde{V}_{:,:,i,j})^{-1}\tilde{V}^*_{:,:,i,j})\tilde{X}_{:,i,j}$ ▷ Apply our parameterization.
end for
$Y := \mathrm{FFT}^{-1}(\tilde{Y})$
Return $(Y_{:,k:-k,k:-k})$.real ▷ Extract the real part.

root of the kernel, significantly prolonging training time and increasing memory usage. Conversely, the matrix operations in BRO are less complex, leading to substantially less training time and memory usage. Moreover, the low-rank parametrization characteristic of BRO further alleviates the demand for computational resources. When comparing BRO to SOC, BRO has an advantage in terms of inference time, as SOC requires multiple convolution operations to compute the exponential convolution. Figure 2 shows the runtime per epoch and the memory usage during training. A detailed analysis and comparison of orthogonal layers, including Cayley, are provided in Appendix A.5.

Non-universal Orthogonal Parameterization While a single BRO layer is not a universal approximator for orthogonal layers, as established in the second property of Proposition 1, we empirically demonstrate in Section 6.2 that the expressive power of deep neural networks constructed using BRO is competitive with that of LOT and SOC.

5. Logit Annealing Loss Function

Singla et al. (2022) posited that cross-entropy (CE) loss is inadequate for training Lipschitz models, as it fails to increase the margin. Thus, they integrated Certificate Regularization (CR) with the CE loss, formulated as: $\mathcal{L}_{\text{CE}} - \gamma \max(\mathcal{M}_f(x), 0)$, where $\mathcal{M}_f(x) = f(x)_t - \max_{k\neq t} f(x)_k$ is the logit margin between the ground-truth class t and the runner-up class. $\gamma \max(\mathcal{M}_f(x), 0)$ is the CR term and γ is a hyper-parameter. However, our investigation identifies several critical issues associated with the CR term, such as discontinuous loss gradient and gradient domination. Refer to Appendix C.3 for details.

Our insight reveals that Lipschitz neural networks inherently possess limited model complexity, which impedes empirical risk minimization. Here, we utilize Rademacher complexity to justify that the empirical margin loss risk (Bartlett et al., 2017) is challenging to minimize with Lipschitz neural networks. Let $\mathcal{H}$ represent the hypothesis set. The empirical Rademacher complexity of $\mathcal{H}$ over a set $S = \{x_1, x_2, \ldots, x_n\}$ is given by:

$$\mathfrak{R}_S(\mathcal{H}) = \mathbb{E}_\sigma \left[\sup_{h\in\mathcal{H}} \frac{1}{n} \sum_{i=1}^{n} \sigma_i h(x_i) \right], \tag{3}$$

where σ_i are independent Rademacher variables uniformly sampled from $\{-1, 1\}$. Next, we use the Rademacher complexity to demonstrate that a model with low capacity results in a greater lower bound for margin loss risk.

Theorem 1. *Given a neural network f and a set S of size n, let ℓ_τ denote the ramp loss (a special margin loss, see Appendix C) (Bartlett et al., 2017). Let $\mathcal{F}$ represent the hypothesis set of f. Define that:*

$$\mathcal{F}_\tau := \{(x, y) \mapsto \ell_\tau(\mathcal{M}(f(x), y))) : f \in \mathcal{F}\}; \tag{4}$$

$$\hat{\mathcal{R}}_\tau(f) := \frac{\sum_i \ell_\tau(\mathcal{M}(f(x_i), y_i))}{n}. \tag{5}$$

Assume that $\mathcal{P}_e$ is the prediction error probability. Then, with probability $1 - \delta$, the empirical margin loss risk $\hat{\mathcal{R}}_\tau(f)$ is lower bounded by:

$$\hat{\mathcal{R}}_\tau(f) \geq \mathcal{P}_e - 2\mathfrak{R}_S(\mathcal{F}_\tau) - 3\sqrt{\frac{\ln(1/\delta)}{2n}}. \tag{6}$$

Furthermore, for the L-Lipschitz neural networks, we introduce the following inequality to show that the model complexity is upper-bounded by L.

Proposition 3. *(Ledoux & Talagrand, 2013) Let $\mathcal{F}$ be the hypothesis set of the L-Lipschitz neural network f, and ℓ_τ is the ramp loss with Lipschitz constant $1/\tau$, for some $\tau > 0$. Then, given a set S of size n, we have:*

$$\begin{aligned}
\mathfrak{R}_S(\mathcal{F}_\tau) &= \mathbb{E}_\sigma \left[\frac{1}{n} \sup_{f\in\mathcal{F}} \sum_{i=1}^{n} \sigma_i (\ell_\tau \circ f)(x_i) \right] \\
&\leq \frac{1}{\tau} \mathbb{E}_\sigma \left[\frac{1}{n} \sup_{f\in\mathcal{F}} \sum_{i=1}^{n} \sigma_i f(x_i) \right] \\
&\leq \frac{L}{\tau \cdot n} \sum_{i=1}^{n} ||x_i||.
\end{aligned} \tag{7}$$

Table 1. Comparison of the proposed method with previous works. The ℓ_2 perturbation budget ε for certified accuracy is chosen following the convention of previous works. † For fair comparison, no additional diffusion-generated synthetic datasets are used during training.

Datasets	**Models**	**#Param.**	**Clean Acc.**	**Certified Acc. (ε)**		
				$\frac{36}{255}$	$\frac{72}{255}$	$\frac{108}{255}$
CIFAR-10	Cayley Large (Trockman & Kolter, 2021)	21M	74.6	61.4	46.4	32.1
	SOC-20 (Singla et al., 2022)	27M	76.3	62.6	48.7	36.0
	LOT-20 (Xu et al., 2022)	18M	77.1	64.3	49.5	36.3
	CPL XL (Meunier et al., 2022)	236M	78.5	64.4	48.0	33.0
	AOL Large (Prach & Lampert, 2022)	136M	71.6	64.0	56.4	**49.0**
	SOC-20+CRC (Singla & Feizi, 2022)	40M	79.1	66.5	52.5	38.1
	SLL X-Large (Araujo et al., 2023)	236M	73.3	64.8	55.7	47.1
	LiResNet† (Hu et al., 2024)	83M	81.0	69.8	56.3	42.9
	BRONet-M	37M	80.5	68.9	56.3	42.7
	BRONet-L	68M	81.0	70.2	57.1	43.0
	BRONet-M (+LA)	37M	81.2	69.7	55.6	40.7
	BRONet-L (+LA)	68M	**81.6**	**70.6**	**57.2**	42.5
CIFAR-100	Cayley Large (Trockman & Kolter, 2021)	21M	43.3	29.2	18.8	11.0
	SOC-20 (Singla et al., 2022)	27M	47.8	34.8	23.7	15.8
	LOT-20 (Xu et al., 2022)	18M	48.8	35.2	24.3	16.2
	CPL XL (Meunier et al., 2022)	236M	47.8	33.4	20.9	12.6
	AOL Large (Prach & Lampert, 2022)	136M	43.7	33.7	26.3	20.7
	SOC-20+CRC (Singla & Feizi, 2022)	40M	51.8	38.5	27.2	18.5
	SLL X-Large (Araujo et al., 2023)	236M	47.8	36.7	28.3	**22.2**
	Sandwich (Wang & Manchester, 2023)	26M	46.3	35.3	26.3	20.3
	LiResNet† (Hu et al., 2024)	83M	53.0	**40.2**	28.3	19.2
	BRONet-M	37M	53.3	40.0	28.3	19.2
	BRONet-L	68M	53.6	**40.2**	28.6	19.2
	BRONet-M (+LA)	37M	54.1	40.1	28.5	19.6
	BRONet-L (+LA)	68M	**54.3**	**40.2**	**29.1**	20.3
ImageNet	LiResNet† (Hu et al., 2024)	98M	47.3	35.3	25.1	16.9
	BRONet	86M	48.8	36.4	25.8	17.5
	BRONet (+LA)	86M	**49.3**	**37.6**	**27.9**	**19.6**

This is also known as Ledoux-Talagrand contraction (Ledoux & Talagrand, 2013). In Lipschitz neural networks, the upper bound is typically lower than in standard networks due to the smaller Lipschitz constant L, consequently limiting $\mathfrak{R}_S(\mathcal{F}_\tau)$.

According to Theorem 1, the empirical margin loss risk exhibits a greater lower bound if $\mathfrak{R}_S(\mathcal{F}_\tau)$ is low. It is important to note that the risk of the CR term, i.e., CR loss risk, is exactly the margin loss risk decreased by one unit when $\tau = 1/\gamma$. That is $\hat{\mathcal{R}}_{CR}(f) = \hat{\mathcal{R}}_\tau(f) - 1$. This indicates that CR loss risk also exhibits a greater lower bound. Thus, it is unlikely to minimize the CR term indefinitely if the model exhibits limited Rademacher complexity. Note that limited Rademacher complexity can result from a low Lipschitz constant or a large sample set. This also implies that we cannot limitlessly enlarge the margin in Lipschitz networks, especially for large real-world datasets. Detailed proofs can be found in Appendix C.

The CR term encourages a large margin for every data point simultaneously, which is unlikely since the risk has a great lower bound. Due to the limited capacity of Lipschitz models, we must design a mechanism that enables models to learn appropriate margins for most data points. Specifically, when a data point exhibits a large margin, indicating further optimizing it is less beneficial, its loss should be annealed to allocate capacity for other data points. Based on this idea, we design a logit annealing mechanism to modulate the learning process, gradually reducing loss values of the large-margin data points. Consequently, we propose a novel loss function: the *Logit Annealing* (LA) loss. Let $\boldsymbol{z} = f(x)$ represent the logits output by the neural network, and let $\boldsymbol{y}$ be the one-hot encoding of the true label t. We define the LA loss as follows:

$$\mathcal{L}_{\mathrm{LA}}(\boldsymbol{z}, \boldsymbol{y}) = -T(1-\boldsymbol{p}_t)^\beta \log(\boldsymbol{p}_t), \quad \text{where } \boldsymbol{p} = \mathrm{softmax}\left(\frac{\boldsymbol{z}-\xi\boldsymbol{y}}{T}\right). \tag{8}$$

Table 2. Improvements of LA and BRONet compared to LiResNet using diffusion data augmentation. The best results of each dataset are marked in bold. Performance improvements and degradations relative to the baseline are marked in green and red, respectively.

Datasets	**Methods**	**Clean Acc.**	**Certified Acc. (ε)**		
			$\frac{36}{255}$	$\frac{72}{255}$	$\frac{108}{255}$
CIFAR-10 (+EDM 4M)	LiResNet	87.0	78.1	66.1	53.1
	+LA	86.7 (-0.3)	78.1 (+0.0)	67.0 (+0.9)	54.2 (+1.1)
	BRONet+LA	**87.2** (+0.2)	**78.3** (+0.2)	**67.4** (+1.3)	**54.5** (+1.4)
CIFAR-100 (+EDM 1M)	LiResNet	61.0	48.4	36.9	26.5
	+LA	61.1 (+0.1)	48.9 (+0.5)	37.5 (+0.6)	**27.6** (+1.1)
	BRONet+LA	**61.6** (+0.6)	**49.1** (+0.7)	**37.7** (+0.8)	27.2 (+0.7)
ImageNet (+EDM2 2M)	LiResNet	50.9	38.4	27.6	18.9
	+LA	51.0 (+0.1)	39.4 (+1.0)	29.2 (+1.6)	20.6 (+1.7)
	BRONet+LA	**52.3** (+1.4)	**40.7** (+2.3)	**30.3** (+2.7)	**21.6** (+2.7)

The hyper-parameters temperature T and offset ξ are adapted from the loss function in Prach & Lampert (2022) for margin training. The term $(1 - \boldsymbol{p}_t)^{\beta}$, referred to as the annealing mechanism, draws inspiration from the Focal Loss (Lin et al., 2017). During training, the LA loss initially promotes a moderate margin for each data point, subsequently annealing the data points with large margins as training progresses. Unlike the CR term, which encourages aggressive margin maximization, our method employs a balanced learning strategy that effectively utilizes the model's capacity, especially when it is limited. Consequently, the LA loss allows Lipschitz models to learn an appropriate margin for most data points. Appendix C provides more details on the LA loss.

6. Experiments

In this section, we first evaluate the overall performance of our proposed BRONet against the ℓ_2 certified robustness baselines. Next, to further demonstrate the effectiveness of the BRO layer, we conduct fair and comprehensive evaluations on multiple architectures for comparative analysis with orthogonal and other Lipschitz layers in previous literature. Lastly, we present the experimental results and analysis on the LA loss. See Appendix B for implementation details.

6.1. Main Results

We compare BRONet to the current leading methods in the literature. Figure 1 presents a visual comparison on CIFAR-10. The circle size indicates the number of model parameters. Furthermore, Table 1 details the clean accuracy, certified accuracy, as well as the total number of parameters. For reference, we present the results of the proposed BRONet both with and without the LA loss function. On CIFAR-10 and CIFAR-100, our model achieves the best clean and certified accuracy with the ℓ_2 perturbation budget $\varepsilon = 36/255$. On the ImageNet dataset, our method achieves state-of-the-art performance, highlighting its scalability. Notably, BRONets attain these results with a reasonable number of parameters. Additional results for the Tiny-ImageNet experiments are provided in Appendix D.1.

6.2. Ablation Studies

Extra Diffusion Data Augmentation As demonstrated in previous studies (Hu et al., 2024; Wang et al., 2023), incorporating additional synthetic data generated by diffusion models such as elucidating diffusion model (EDM) (Karras et al., 2022) can enhance performance. We evaluate the effectiveness of our method in this setting, using synthetic datasets publicly released from Hu et al. (2024); Wang et al. (2023) for CIFAR-10 and CIFAR-100, which contain post-filtered 4 million and 1 million images, respectively. For ImageNet, we generate 2 million 512x512 images using the script recommended by EDM2 with autoguidance (Karras et al., 2024b;a). Table 2 presents the results, showing that combining LA and BRO effectively leverages these synthetic datasets to enhance performance.

Backbone Comparison As the improvements in the previous work by Hu et al. (2024) primarily stem from using diffusion-generated synthetic datasets and architectural changes, we conduct a fair and comprehensive comparison of different Lipschitz convolutional layers using the default LiResNet architecture (with Lipschitz-regularized convolutional layers), along with LA and diffusion-based data augmentation. The only modification is swapping out the convolutional backbone layers. It is important to note that for FFT-based orthogonal layers (excluding BRO), we must reduce the number of backbone layers to stay within memory constraints. LOT has the fewest parameters due to its costly parameterization. With half-rank parameterization in BRO, the number of parameters for BRO, Cayley, and

Table 3. Comparison of clean and certified accuracy using different Lipschitz convolutional backbones. The best results are marked in bold. #Layers is the number of convolutional backbone layers, and #param. is the number of parameters in the constructed architecture.

Conv. Backbone	#Layers	#Param.	CIFAR-10 (+EDM)				CIFAR-100 (+EDM)			
			Clean	$\frac{36}{255}$	$\frac{72}{255}$	$\frac{108}{255}$	Clean	$\frac{36}{255}$	$\frac{72}{255}$	$\frac{108}{255}$
LOT	2	59M	85.7	76.4	65.1	52.2	59.4	47.6	36.6	26.3
Cayley	6	68M	86.7	77.7	66.9	54.3	61.1	48.7	**37.8**	27.5
Cholesky	6	68M	85.4	76.6	65.7	53.3	59.4	47.4	36.8	26.9
SLL	12	83M	85.6	76.8	66.0	53.3	59.4	47.6	36.6	27.0
SOC	12	83M	86.6	78.2	67.0	54.1	60.9	48.9	37.6	**27.8**
Lip-reg	12	83M	86.7	78.1	67.0	54.2	61.1	48.9	37.5	27.6
BRO	12	68M	**87.2**	**78.3**	**67.4**	**54.5**	**61.6**	**49.1**	37.7	27.2

Table 4. Comparison of clean and certified accuracy with different orthogonal layers in LipConvNets (Depth-Width). Instances marked with a dash (-) indicate out of memory during training. The best results with each model are marked with bold.

Model	D-W	Layer	CIFAR-100				Tiny-ImageNet			
			Clean	$\frac{36}{255}$	$\frac{72}{255}$	$\frac{108}{255}$	Clean	$\frac{36}{255}$	$\frac{72}{255}$	$\frac{108}{255}$
LipConvNet (+LA)	(10–32)	SOC	47.5	34.7	24.0	15.9	38.0	26.5	17.7	11.3
		LOT	**49.1**	**35.5**	24.4	**16.3**	**40.2**	27.9	**18.7**	**11.8**
		BRO	48.6	35.4	**24.5**	16.1	39.4	**28.1**	18.2	11.6
	(10–48)	SOC	48.2	34.9	24.4	16.2	38.9	27.1	17.6	11.2
		LOT	**49.4**	35.8	24.8	16.3	–	–	–	–
		BRO	**49.4**	**36.2**	**24.9**	**16.7**	**40.0**	**28.1**	**18.9**	**12.3**
	(10–64)	SOC	48.5	35.5	24.4	16.3	39.3	27.3	17.6	11.2
		LOT	49.6	36.1	24.7	16.2	–	–	–	–
		BRO	**49.7**	**36.7**	**25.2**	**16.8**	**40.7**	**28.4**	**19.2**	**12.5**

Table 5. Ablation study on the components contributing to the improvement on the **ImageNet** dataset.

LA	Arch	BRO	Clean Acc.	Certified Acc. (ε)		
				$\frac{36}{255}$	$\frac{72}{255}$	$\frac{108}{255}$
✗	✗	✗	47.3	35.3	25.1	16.9
✓	✗	✗	47.8	36.6	26.7	18.7
✓	✓	✗	48.8	37.1	26.8	18.8
✓	✓	✓	**49.3**	**37.6**	**27.9**	**19.6**

Cholesky remain consistent, while SLL, SOC, and Lipschitz-regularized retain the original number of parameters. The results in Table 3 indicate that BRO is the optimal choice compared to other layers in terms of overall performance.

LipConvNet Benchmark To further validate the effectiveness of BRO, we evaluate it on LipConvNets, a standard lightweight architecture widely used in the literature on orthogonal layers. Table 4 illustrates the certified robustness of SOC, LOT, and BRO layers. It is evident that the LipConvNet constructed by BRO layers compares favorably to the other orthogonal layers. Furthermore, due to the nature of its low-rank parametrization property, BRO layers require the fewest parameters and reasonable runtime. Detailed comparisons are provided in Appendix D.6.

Improvement on ImageNet Compared to LiResNet on ImageNet, we have made three key modifications: introducing the BRO convolutional layers, incorporating the LA loss, and making an architectural adjustment—replacing the 1-Lipschitz learnable downsampling layer with norm-preserving ℓ_2-norm pooling. Table 5 presents the ablation study on the components, demonstrating that the combination of all three components yields the best performance.

6.3. LA Loss Effectiveness

Table 1, 2, and 5 illustrates the performance improvements achieved using the proposed LA loss. We also provide extensive ablation experiments in Appendix D.4 to validate its effectiveness on LipConvNets. Our experiments show that the LA loss promotes a balanced margin, especially for models trained on more challenging datasets.

Table 6. The statistics of certified radius distribution.

Loss	Median	Variance	Skewness
CE	0.2577	0.0732	1.2114
CE+CR	0.2750	0.1000	1.4843
LA	0.2840	0.0797	1.0539

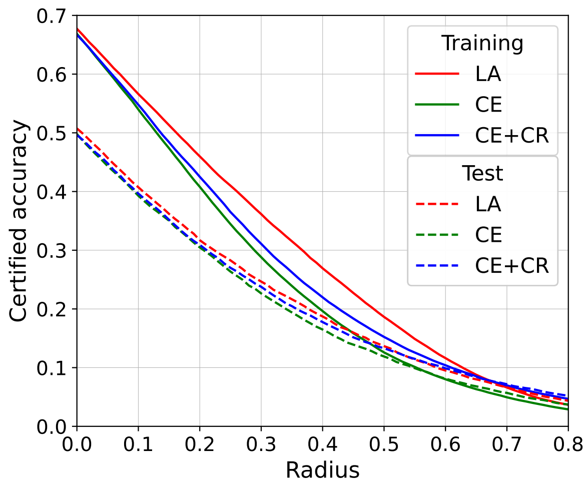

Figure 3. Certified accuracy with respect to radius. The LA loss helps learn appropriate margin.

To demonstrate that the LA loss enables learning an appropriate margin for most data points, we further investigate the certified radius distribution. Following Cohen et al. (2019), we plot the certified accuracy with respect to the radius on CIFAR-100 to visualize the margin distribution in Figure 3. The certified radius is proportional to the margin in Lipschitz models. Thus, the x-axis and y-axis can be seen as margin and complementary cumulative distribution of data points, respectively (Lecuyer et al., 2019).

The results indicate that the number of data points with appropriate margins increases, which is evident as the red curve rises higher than the others at the radius between $[0.0, 0.6]$. Moreover, the clean accuracy, which corresponds to certified accuracy at zero radius, is also observed to be slightly higher. This suggests that the LA loss does not compromise clean accuracy for robustness. To better characterize the annealing mechanism, we analyze the distribution of the certified radius across the data points, as shown in Table 6. Compared to CR, the LA loss reduces both the positive skewness and variance of the distribution, indicating a rightward shift in the peak and a decrease in the dispersion of the radius. This suggests that LA loss helps mitigate the issue of overfitting to certain data points and improves the certified radius for most points. Additional experiments, including ablation studies on BRO rank and the LA loss, are presented in Appendix D.

7. Conclusion

In this paper, we introduce a novel BRO layer that features low-rank parameterization and is free from iterative approximations. As a result, it is both memory and time efficient compared to existing orthogonal layers, making it well-suited for integration into advanced Lipschitz architectures. Furthermore, comprehensive experimental results have shown that BRO is one of the most promising orthogonal convolutional layers for constructing expressive Lipschitz networks. Next, we address the limited complexity issue of Lipschitz neural networks and introduce the new Logit Annealing loss function to help models learn appropriate margins. Extensive experiments on CIFAR-10, CIFAR-100, Tiny-ImageNet, and ImageNet validate the effectiveness of the proposed methods over existing baselines. Moving forward, the principles and methodologies in this paper could serve as a foundation for future research in certifiably robust network design.

Acknowledgment

This work was supported in part by the National Science and Technology Council (NSTC) under Grants NSTC 113-2222-E-002-004-MY3, NSTC 113-2634-F-002-007, NSTC 113-2634-F-002-001-MBK, and NSTC 113-2923-E-002-010-MY2, as well as by the Featured Area Research Center Program within the Higher Education Sprout Project of the Ministry of Education (Grant 113L900903). In addition, we thank the National Center for High-performance Computing (NCHC) for providing computational and storage resources. We also appreciate the constructive comments received from anonymous reviewers, which substantially improved both the clarity and depth of our presentation.

Impact Statement

This work aims to enhance the robustness and reliability of deep neural networks, ultimately contributing to the development of trustworthy AI systems. Consequently, it has the potential for positive societal impact. However, we also recognize two potential negative implications. The first concern is adversarial misuse. While this method improves the robustness and reliability of machine learning models, there is a risk that it could be exploited for malicious purposes. For example, more secure and robust models might be weaponized in applications such as surveillance systems or autonomous malicious agents. The second concern relates to resource utilization. Although this method is more memory-efficient than other approaches, the overall computational and energy costs associated with large-scale deployment still need to be considered, particularly in cloud computing environments.

References

Achour, E. M., Malgouyres, F., and Mamalet, F. Existence, stability and scalability of orthogonal convolutional neural networks. *Journal of Machine Learning Research (JMLR)*, 2022.

Anil, C., Lucas, J., and Grosse, R. Sorting out Lipschitz function approximation. In *International Conference on Machine Learning (ICML)*, 2019.

Araujo, A., Havens, A. J., Delattre, B., Allauzen, A., and Hu, B. A unified algebraic perspective on Lipschitz neural networks. In *International Conference on Learning Representations (ICLR)*, 2023.

Bartlett, P. L., Foster, D. J., and Telgarsky, M. J. Spectrally-normalized margin bounds for neural networks. In *Advances in Neural Information Processing Systems (NeurIPS)*, 2017.

Béthune, L., Boissin, T., Serrurier, M., Mamalet, F., Friedrich, C., and Gonzalez Sanz, A. Pay attention to your loss: understanding misconceptions about Lipschitz neural networks. In *Advances in Neural Information Processing Systems (NeurIPS)*, 2022.

Brown, T., Mann, B., Ryder, N., Subbiah, M., Kaplan, J. D., Dhariwal, P., Neelakantan, A., Shyam, P., Sastry, G., Askell, A., et al. Language models are few-shot learners. In *Advances in Neural Information Processing Systems (NeurIPS)*, 2020.

Carlini, N. and Wagner, D. Audio adversarial examples: Targeted attacks on speech-to-text. In *IEEE security and privacy workshops (SPW)*, 2018.

Chen, T., Zhang, Z., Liu, S., Chang, S., and Wang, Z. Robust overfitting may be mitigated by properly learned smoothening. In *International Conference on Learning Representations (ICLR)*, 2021.

Chernodub, A. and Nowicki, D. Norm-preserving orthogonal permutation linear unit activation functions (OPLU). *arXiv preprint arXiv:1604.02313*, 2016.

Cohen, J., Rosenfeld, E., and Kolter, Z. Certified adversarial robustness via randomized smoothing. In *International Conference on Machine Learning (ICML)*, 2019.

Croce, F. and Hein, M. Reliable evaluation of adversarial robustness with an ensemble of diverse parameter-free attacks. In *International Conference on Machine Learning (ICML)*, 2020.

Das, N., Shanbhogue, M., Chen, S.-T., Hohman, F., Li, S., Chen, L., Kounavis, M. E., and Chau, D. H. Shield: Fast, practical defense and vaccination for deep learning using jpeg compression. In *Proceedings of the 24th ACM SIGKDD International Conference on Knowledge Discovery & Data Mining (KDD)*, 2018.

Dietrich, G. A new formulation of the hypermatrix householder-QR decomposition. *Computer Methods in Applied Mechanics and Engineering*, 9(3):273–280, 1976.

Dozat, T. Incorporating Nesterov momentum into Adam. *International Conference on Learning Representations workshop (ICLR workshop)*, 2016.

Ehlers, R. Formal verification of piece-wise linear feed-forward neural networks. In *International Symposium on Automated Technology for Verification and Analysis (ATVA)*, 2017.

Engstrom, L., Ilyas, A., and Athalye, A. Evaluating and understanding the robustness of adversarial logit pairing. *arXiv preprint arXiv:1807.10272*, 2018.

Farnia, F., Zhang, J., and Tse, D. Generalizable adversarial training via spectral normalization. In *International Conference on Learning Representations (ICLR)*, 2019.

Fazlyab, M., Robey, A., Hassani, H., Morari, M., and Pappas, G. Efficient and accurate estimation of Lipschitz constants for deep neural networks. In *Advances in Neural Information Processing Systems (NeurIPS)*, 2019.

Goodfellow, I. J., Shlens, J., and Szegedy, C. Explaining and harnessing adversarial examples. *arXiv preprint arXiv:1412.6572*, 2014.

Gowal, S., Dvijotham, K., Stanforth, R., Bunel, R., Qin, C., Uesato, J., Arandjelovic, R., Mann, T., and Kohli, P. On the effectiveness of interval bound propagation for training verifiably robust models. *arXiv preprint arXiv:1810.12715*, 2018.

He, K., Zhang, X., Ren, S., and Sun, J. Delving deep into rectifiers: Surpassing human-level performance on imagenet classification. In *Proceedings of the IEEE International Conference on Computer Vision (ICCV)*, 2015.

Hu, E. J., Wallis, P., Allen-Zhu, Z., Li, Y., Wang, S., Wang, L., Chen, W., et al. Lora: Low-rank adaptation of large language models. In *International Conference on Learning Representations (ICLR)*, 2022.

Hu, K., Zou, A., Wang, Z., Leino, K., and Fredrikson, M. Unlocking deterministic robustness certification on Imagenet. In *Advances in Neural Information Processing Systems (NeurIPS)*, 2023.

Hu, K., Leino, K., Wang, Z., and Fredrikson, M. A recipe for improved certifiable robustness. In *The Twelfth International Conference on Learning Representations (ICLR)*, 2024.

Jain, A. K. *Fundamentals of digital image processing*. Prentice-Hall, Inc., 1989.

Karras, T., Aittala, M., Aila, T., and Laine, S. Elucidating the design space of diffusion-based generative models. In *Advances in Neural Information Processing Systems (NeurIPS)*, 2022.

Karras, T., Aittala, M., Kynkäänniemi, T., Lehtinen, J., Aila, T., and Laine, S. Guiding a diffusion model with a bad version of itself. In *Advances in Neural Information Processing Systems (NeurIPS)*, 2024a.

Karras, T., Aittala, M., Lehtinen, J., Hellsten, J., Aila, T., and Laine, S. Analyzing and improving the training dynamics of diffusion models. In *Proceedings of the IEEE/CVF Conference on Computer Vision and Pattern Recognition (CVPR)*, 2024b.

Lecuyer, M., Atlidakis, V., Geambasu, R., Hsu, D., and Jana, S. Certified robustness to adversarial examples with differential privacy. In *2019 IEEE Symposium on Security and Privacy (SP)*, 2019.

Ledoux, M. and Talagrand, M. *Probability in Banach Spaces: isoperimetry and processes*. Springer Science & Business Media, 2013.

Lee, M. and Kim, D. Robust evaluation of diffusion-based adversarial purification. In *Proceedings of the IEEE/CVF International Conference on Computer Vision (ICCV)*, 2023.

Leino, K., Wang, Z., and Fredrikson, M. Globally-robust neural networks. In *International Conference on Machine Learning (ICML)*, 2021.

Li, L., Xie, T., and Li, B. Sok: Certified robustness for deep neural networks. In *2023 IEEE symposium on security and privacy (SP)*, 2023.

Li, Q., Haque, S., Anil, C., Lucas, J., Grosse, R. B., and Jacobsen, J.-H. Preventing gradient attenuation in Lipschitz constrained convolutional networks. In *Advances in Neural Information Processing Systems (NeurIPS)*, 2019.

Lin, T.-Y., Goyal, P., Girshick, R., He, K., and Dollar, P. Focal loss for dense object detection. In *Proceedings of the IEEE International Conference on Computer Vision (ICCV)*, 2017.

Madry, A., Makelov, A., Schmidt, L., Tsipras, D., and Vladu, A. Towards deep learning models resistant to adversarial attacks. In *International Conference on Learning Representations (ICLR)*, 2018.

Mao, Y., Müller, M., Fischer, M., and Vechev, M. Connecting certified and adversarial training. In *Advances in Neural Information Processing Systems (NeurIPS)*, 2023.

Meunier, L., Delattre, B. J., Araujo, A., and Allauzen, A. A dynamical system perspective for Lipschitz neural networks. In *International Conference on Machine Learning (ICML)*, 2022.

Mohri, M., Rostamizadeh, A., and Talwalkar, A. *Foundations of machine learning*. MIT press, 2018.

Mueller, M. N., Eckert, F., Fischer, M., and Vechev, M. Certified training: Small boxes are all you need. In *The Eleventh International Conference on Learning Representations (ICLR)*, 2023.

Müller, J., Klein, R., and Weinmann, M. Orthogonal wasserstein gans. *arXiv preprint arXiv:1911.13060*, 2019.

Paszke, A., Gross, S., Massa, F., Lerer, A., Bradbury, J., Chanan, G., Killeen, T., Lin, Z., Gimelshein, N., Antiga, L., et al. Pytorch: An imperative style, high-performance deep learning library. In *Advances in Neural Information Processing Systems (NeurIPS)*, 2019.

Prach, B. and Lampert, C. H. Almost-orthogonal layers for efficient general-purpose Lipschitz networks. In *European Conference on Computer Vision (ECCV)*, 2022.

Prach, B., Brau, F., Buttazzo, G., and Lampert, C. H. 1-Lipschitz layers compared: Memory, speed, and certifiable robustness. *arXiv preprint arXiv:2311.16833*, 2023.

Qi, H., You, C., Wang, X., Ma, Y., and Malik, J. Deep isometric learning for visual recognition. In *International Conference on Machine Learning (ICML)*, 2020.

Samangouei, P., Kabkab, M., and Chellappa, R. Defense-gan: Protecting classifiers against adversarial attacks using generative models. In *International Conference on Learning Representations (ICLR)*, 2018.

Schönemann, P. H. A generalized solution of the orthogonal procrustes problem. *Psychometrika*, 31(1):1–10, 1966.

Schreiber, R. and Parlett, B. Block reflectors: Theory and computation. *SIAM Journal on Numerical Analysis*, 25 (1):189–205, 1988.

Shafahi, A., Najibi, M., Ghiasi, M. A., Xu, Z., Dickerson, J., Studer, C., Davis, L. S., Taylor, G., and Goldstein, T. Adversarial training for free! In *Advances in Neural Information Processing Systems (NeurIPS)*, 2019.

Shi, Z., Wang, Y., Zhang, H., Kolter, J. Z., and Hsieh, C.-J. Efficiently computing local Lipschitz constants of neural networks via bound propagation. In *Advances in Neural Information Processing Systems (NeurIPS)*, 2022.

Singla, S. and Feizi, S. Fantastic four: Differentiable bounds on singular values of convolution layers. In *International Conference on Learning Representations (ICLR)*, 2021a.

Singla, S. and Feizi, S. Skew orthogonal convolutions. In *International Conference on Machine Learning (ICML)*, 2021b.

Singla, S. and Feizi, S. Improved techniques for deterministic l2 robustness. In *Advances in Neural Information Processing Systems (NeurIPS)*, 2022.

Singla, S., Singla, S., and Feizi, S. Improved deterministic l2 robustness on CIFAR-10 and CIFAR-100. In *International Conference on Learning Representations (ICLR)*, 2022.

Szegedy, C., Zaremba, W., Sutskever, I., Bruna, J., Erhan, D., Goodfellow, I., and Fergus, R. Intriguing properties of neural networks. In *International Conference on Learning Representations (ICLR)*, 2014.

Trockman, A. and Kolter, J. Z. Orthogonalizing convolutional layers with the Cayley transform. In *International Conference on Learning Representations (ICLR)*, 2021.

Tsuzuku, Y., Sato, I., and Sugiyama, M. Lipschitz-margin training: Scalable certification of perturbation invariance for deep neural networks. In *Advances in Neural Information Processing Systems (NeurIPS)*, 2018.

Virmaux, A. and Scaman, K. Lipschitz regularity of deep neural networks: analysis and efficient estimation. In *Advances in Neural Information Processing Systems (NeurIPS)*, 2018.

Wang, C.-Y., Bochkovskiy, A., and Liao, H.-Y. M. Yolov7: Trainable bag-of-freebies sets new state-of-the-art for real-time object detectors. *arXiv preprint arXiv:2207.02696*, 2022.

Wang, R. and Manchester, I. Direct parameterization of Lipschitz-bounded deep networks. In *International Conference on Machine Learning (ICML)*, 2023.

Wang, S., Zhang, H., Xu, K., Lin, X., Jana, S., Hsieh, C.-J., and Kolter, J. Z. Beta-crown: Efficient bound propagation with per-neuron split constraints for neural network robustness verification. In *Advances in Neural Information Processing Systems (NeurIPS)*, 2021.

Wang, Z., Pang, T., Du, C., Lin, M., Liu, W., and Yan, S. Better diffusion models further improve adversarial training. In *International Conference on Machine Learning (ICML)*, 2023.

Xiao, L., Bahri, Y., Sohl-Dickstein, J., Schoenholz, S., and Pennington, J. Dynamical isometry and a mean field theory of cnns: How to train 10,000-layer vanilla convolutional neural networks. In *International Conference on Machine Learning (ICML)*, 2018.

Xu, X., Li, L., and Li, B. Lot: Layer-wise orthogonal training on improving l2 certified robustness. In *Advances in Neural Information Processing Systems (NeurIPS)*, 2022.

Yang, G., Duan, T., Hu, J. E., Salman, H., Razenshteyn, I., and Li, J. Randomized smoothing of all shapes and sizes. In *International Conference on Machine Learning (ICML)*, 2020.

Yu, T., Li, J., Cai, Y., and Li, P. Constructing orthogonal convolutions in an explicit manner. In *International Conference on Learning Representations (ICLR)*, 2022.

Zhang, H., Wang, S., Xu, K., Li, L., Li, B., Jana, S., Hsieh, C.-J., and Kolter, J. Z. General cutting planes for bound-propagation-based neural network verification. In *Advances in Neural Information Processing Systems (NeurIPS)*, 2022.

Zhang, M., Lucas, J., Ba, J., and Hinton, G. E. Lookahead optimizer: k steps forward, 1 step back. In *Advances in Neural Information Processing Systems (NeurIPS)*, 2019.

Appendix

Table of Contents

A. BRO Layer Analysis

A.1. Proof of Proposition 1

Proposition 1. *Let $V \in \mathbb{R}^{m \times n}$ be a matrix of rank n, and, without loss of generality, assume $m \geq n$. Then the parameterization $W = I - 2V(V^TV)^{-1}V^T$ satisfies the following properties:*

1. *W is orthogonal and symmetric, i.e., $W^T = W$ and $W^TW = I$.*
2. *W is an n-rank perturbation of the identity matrix, i.e., it has n eigenvalues equal to -1 and $m - n$ eigenvalues equal to 1.*
3. *W degenerates to the negative identity matrix when V is a full-rank square matrix.*

Proof. Assuming V is as defined in Proposition 1, the symmetry of this parameterization is straightforward to verify. The orthogonality of W, however, requires confirmation that the following condition is satisfied:

$$\begin{aligned} WW^T &= (I - 2V(V^TV)^{-1}V^T)(I - 2V(V^TV)^{-1}V^T)^T \\ &= (I - 2V(V^TV)^{-1}V^T)(I - 2V(V^TV)^{-1}V^T) \\ &= I - 4V(V^TV)^{-1}V^T + 4V(V^TV)^{-1}V^TV(V^TV)^{-1}V^T \\ &= I - 4V(V^TV)^{-1}V^T + 4V(V^TV)^{-1}V^T \\ &= I. \end{aligned} \tag{9}$$

Next, define $S = \{v_1, v_2, \cdots, v_n\}$ as the set of column vectors of V. Let e_i denote the i-th standard basis vector in $\mathbb{R}^n$. Then, we have

$$\begin{aligned} Wv_i &= (I - 2V(V^TV)^{-1}V^T)v_i \\ &= v_i - 2V(V^TV)^{-1}V^Tv_i \\ &= v_i - 2V(V^TV)^{-1}(V^TVe_i) \\ &= v_i - 2V(V^TV)^{-1}(V^TV)e_i \\ &= v_i - 2Ve_i \\ &= v_i - 2v_i = -v_i. \end{aligned} \tag{10}$$

For the vectors in the orthogonal complement of S, denoted by $S^\perp = \{v_{n+1}, v_{n+2}, \cdots, v_m\}$, we have

$$Wv_i = (I - 2V(V^TV)^{-1}V^T)v_i = v_i. \tag{11}$$

The equality holds because, for all $v_i \in S^\perp$, we have $V^Tv_i = 0$.

Therefore, the eigenspace corresponding to eigenvalue -1 is spanned by S, while the eigenspace corresponding to eigenvalue 1 is spanned by $S^\perp$.

Assume V is a full-rank square matrix, which implies that V is invertible. Thus:

$$\begin{aligned} W &= I - 2V(V^TV)^{-1}V^T \\ &= I - 2VV^{-1}(V^T)^{-1}V^T \\ &= I - 2I \\ &= -I. \end{aligned} \tag{12}$$

Thus, the proof is complete. □

A.2. Proof of Proposition 2

Before providing a rigorous mathematical proof, we first outline the intuitive rationale. To demonstrate that BRO convolution is orthogonal, we show that each component in the convolution pipeline is orthogonal. This pipeline comprises three orthogonal transformations:

1. *Fourier Transform:* Transforms the input from the spatial domain to the Fourier domain.
2. *BRO Matrix Multiplications:* Applies the Block Reflector Orthogonal (BRO) matrices in the Fourier domain.
3. *Inverse Fourier Transform:* Converts the output back to the spatial domain.

Consequently, the input undergoes a sequence of orthogonal operations, ensuring norm preservation. Importantly, an essential part of the analysis is the application of the 2D convolution theorem, which establishes an equivalence between convolution in the spatial domain and pointwise multiplication in the Fourier domain.

Proposition 2. *Let $\tilde{X} = FFT(X) \in \mathbb{C}^{c\times s\times s}$ and $\tilde{V} = FFT(V) \in \mathbb{C}^{c\times n\times s\times s}$, the proposed BRO convolution $Y = FFT^{-1}(\tilde{Y})$, where $\tilde{Y}_{:,i,j} = \tilde{W}_{:,:,i,j}\tilde{X}_{:,i,j}$ and $\tilde{W}_{:,:,i,j} = I - 2\tilde{V}_{:,:,i,j}(\tilde{V}^*_{:,:,i,j}\tilde{V}_{:,:,i,j})^{-1}\tilde{V}^*_{:,:,i,j}$, is a real,* orthogonal *multi-channel 2D circular convolution.*

Proof. To establish the results of Proposition 2, we first present several supporting lemmas.

Lemma 1. *(2D convolution theorem) Let $X, W \in \mathbb{R}^{s\times s}$, and $F \in \mathbb{R}^{s\times s}$ be the DFT matrix. Then, $\tilde{X} = FFT(X) = FXF$, i.e., the DFT is applied to the rows and columns of X. In addition, let the 2D circular convolution of X with W be* $\mathsf{conv}_W(X) \in \mathbb{R}^{s\times s}$. *It follows that*

$$\tilde{W} \odot \tilde{X} = FWF \odot FXF = F\mathsf{conv}_W(X)F,$$

where $\odot$ is the element-wise product.

Next, we introduce the multi-channels 2D circular convolution. Following Trockman & Kolter (2021), we flatten the four-dimension tensors into matrices to facilitate the analysis. Let an input image with c_{in} input channels represent $X \in \mathbb{R}^{c_{\mathsf{in}}\times s\times s}$, it can be vectorized into $\mathcal{X} = [\mathrm{vec}^T(X_1), ..., \mathrm{vec}^T(X_{c_{\mathsf{in}}})]^T \in \mathbb{R}^{c_{\mathsf{in}}s^2}$. Similarly, the vectorized output is $\mathcal{Y} = [\mathrm{vec}^T(Y_1), ..., \mathrm{vec}^T(Y_{c_{\mathsf{out}}})]^T \in \mathbb{R}^{c_{\mathsf{out}}s^2}$. Then, we have a 2D circular convolution operation with $\mathcal{C} \in \mathbb{R}^{c_{\mathsf{out}}s^2\times c_{\mathsf{in}}s^2}$ such that $\mathcal{Y} = \mathcal{C}\mathcal{X}$. Note that $\mathcal{C}$ has $c_{\mathsf{out}} \times c_{\mathsf{in}}$ blocks with size $s^2 \times s^2$.

Lemma 2. *(Trockman & Kolter, 2021, Corollary A.1.1) If $\mathcal{C} \in \mathbb{R}^{c_{\mathsf{out}}s^2\times c_{\mathsf{in}}s^2}$ represents a 2D circular convolution with c_{in} input channels and c_{out} output channels, then it can be block diagonalized as*

$$\mathcal{F}_{c_{\mathsf{out}}}\mathcal{C}\mathcal{F}^*_{c_{\mathsf{in}}} = \mathcal{D}, \tag{13}$$

where $\mathcal{F}_c = S_{c,s^2}(I_c \otimes (F \otimes F))$, S_{c,s^2} is a permutation matrix, I_k is the identity matrix of order k, and $\mathcal{D}$ is block diagonal with s^2 blocks of size $c_{\mathsf{out}} \times c_{\mathsf{in}}$. Note that $\otimes$ is the Kronecker product.

Lemma 3. *Consider $J \in \mathbb{C}^{p\times p}$ as a unitary matrix. Define V and $\tilde{V}$ such that $V = J\tilde{V}J^*$, where $V \in \mathbb{R}^{p\times p}$ and $\tilde{V} \in \mathbb{C}^{p\times p}$. Let* $\mathsf{BRO}(V) = I - 2V(V^*V)^{-1}V^*$ *be our parameterization. Then,*

$$\mathsf{BRO}(V) = J\mathsf{BRO}(\tilde{V})J^*. \tag{14}$$

Proof. Assume J and V are as defined in Lemma 3. Then

$$\begin{aligned} J^*\mathsf{BRO}(V)J &= J^*(I - 2V(V^TV)^{-1}V^T)J \\ &= I - 2(J^*J\tilde{V}J^*)[(J\tilde{V}^*\tilde{V}J^*)]^{-1}(J\tilde{V}^*J^*J) \\ &= I - 2(\tilde{V}J^*)[(J\tilde{V}^*\tilde{V}J^*)]^{-1}(J\tilde{V}^*) \\ &= I - 2\tilde{V}(\tilde{V}^*\tilde{V})^{-1}\tilde{V}^* \qquad (\star) \\ &= \mathsf{BRO}(\tilde{V}). \end{aligned}$$

The equality at $(\star)$ holds because

$$(\tilde{V}^*\tilde{V})^{-1} = J^*(J\tilde{V}^*\tilde{V}J^*)^{-1}J.$$

□

We begin the proof under the assumption that the number of input channels equals the number of output channels, i.e., $c_{\mathsf{in}} = c_{\mathsf{out}} = c$. According to Lemma 2, the stacked weight matrix $\mathcal{C} \in \mathbb{R}^{c_{\text{out}}s^2 \times c_{\text{in}}s^2}$ can be diagonalized as follows:

$$\mathcal{C} = \mathcal{F}_c^* \mathcal{D} \mathcal{F}_c. \tag{15}$$

where $\mathcal{F}_c^*$ and $\mathcal{F}_c$ are unitary matrices, and $\mathcal{D}$ is a block diagonal matrix.

Note that since $\mathcal{D}$ is block diagonal, the BRO transformation of $\mathcal{D}$ can be expressed as:

$$\mathsf{BRO}(\mathcal{D}) = \mathsf{BRO}(\mathcal{D}_1) \oplus \mathsf{BRO}(\mathcal{D}_2) \oplus \cdots \oplus \mathsf{BRO}(\mathcal{D}_{s^2}),$$

where $\oplus$ denotes the direct sum. This is because each block $\mathcal{D}_k$ for $k = 1, \ldots, s^2$ is independently transformed by the BRO operation. Additionally, because the original weight matrix $\mathcal{C}$ is real, the BRO convolution $\mathsf{BRO}(\mathcal{C})$ remains real as well.

Applying Lemma 3 on Equation 15, we consider a real vectorized input $\mathcal{X}$. The output of the BRO convolution is given by:

$$\mathcal{Y} = \mathsf{BRO}(\mathcal{C})\mathcal{X} = \mathcal{F}_c^* \mathsf{BRO}(\mathcal{D}) \mathcal{F}_c \mathcal{X}. \tag{16}$$

This ensures that $\mathcal{Y}$ is real. Consequently, Algorithm 1 is guaranteed to produce a real output when given a real input $\mathcal{X}$.

Finally, the orthogonality of the BRO convolution operation $\mathsf{BRO}(\mathcal{C})$ can be derived as follows. Since both $\mathcal{F}_c^*$ and $\mathcal{F}_c$ are unitary matrices (Trockman & Kolter, 2021), and $\mathsf{BRO}(\mathcal{D})$ is unitary as well, the composition of these unitary operations preserves orthogonality.

Thus, we have established that the BRO convolution operation, $\mathsf{BRO}(\mathcal{C})$, is both orthogonal and real, thereby completing the proof of Proposition 2.

□

A.3. Implementation Details and Analysis of Semi-Orthogonal Layer

To derive the parameterization of semi-orthogonal matrices, we first construct an orthogonal matrix W and then truncate it to the required dimensions. Specifically, for BRO convolution, let the input and output channel sizes be c_{in} and c_{out}, respectively. Define $c = \max(c_{\text{out}}, c_{\text{in}})$. For each index i and j, we parameterize $\tilde{V}_{:,:,i,j} \in \mathbb{C}^{c \times n}$ as $\tilde{W}_{:,:,i,j} \in \mathbb{C}^{c \times c}$, which is then truncated to $\tilde{W}_{:c_{\text{out}},:c_{\text{in}},i,j} \in \mathbb{C}^{c_{\text{out}} \times c_{\text{in}}}$.

In the following, we provide the detailed analysis about semi-orthogonal BRO layers, which can be categorized into two types: dimension expanding layers and dimension reduction layers. To facilitate understanding, we begin with the dense version of BRO (a single 2D matrix).

For a expanding layer constructed with $W \in \mathbb{R}^{d_{\text{out}} \times d_{\text{in}}}$, where $d_{\text{in}} < d_{\text{out}}$, it satisfies the condition $W^T W = I_{d_{\text{in}}}$. Since the condition is equivalent to ensure that the columns are orthonormal, the norm of a vector is preserved when projecting onto its column space, which means $\|Wx\| = \|x\|$ for every $x \in \mathbb{R}^{d_{\text{in}}}$, thus, ensures 1-Lipschitz property.

For a reduction layer constructed with $W \in \mathbb{R}^{d_{\text{out}} \times d_{\text{in}}}$, where $d_{\text{in}} > d_{\text{out}}$, it satisfies the condition $WW^T = I_{d_{\text{out}}}$. Unlike expanding layers, the columns of W in reduction layers cannot be orthonormal due to the dimensionality constraint $d_{\text{in}} > d_{\text{out}}$. Consequently, we have the following relationship for every $x \in \mathbb{R}^{d_{\text{in}}}$, $\|Wx\| \leq \|x\|$. The equality holds if x lies entirely within the subspace spanned by the rows of W. In general, reduction layers do not preserve the norm of input vectors. However, they remain 1-Lipschitz bounded, ensuring that the transformation does not amplify the input norm.

The same principles apply to BRO convolution. The primary difference between the dense and convolution versions of BRO layers arises from the dimensions they are applied to. Therefore, the results discussed for BRO dense layers also hold for BRO convolution layers. Figure 4 visualizes BRO convolution under three different dimensional settings, illustrating the behavior of channel-expanding and channel-reduction operations in convolutional contexts.

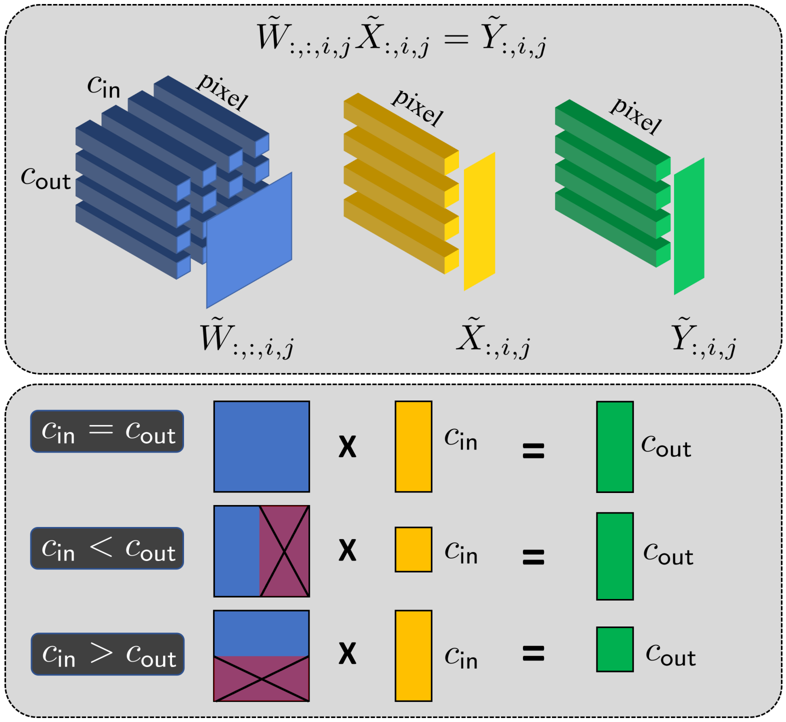

Figure 4. Visualization of BRO convolution for different c_{in} and c_{out}.

A.4. The Implementation and Effect of Zero-padding

Following Xu et al. (2022), we apply zero-padding on images $X \in \mathbb{R}^{c\times s\times s}$, creating $X_{\text{pad}} \in \mathbb{R}^{c\times(s+2k')\times(s+2k')}$, before performing the 2D FFT. After applying FFT^{-1}, we obtain $Y_{\text{pad}} \in \mathbb{R}^{c\times(s+2k')\times(s+2k')}$, from which the padded pixels are removed to restore the original dimensions of X, resulting in $Y \in \mathbb{R}^{c\times s\times s}$. This approach leverages zero-padding to alleviate the effect of circular convolution across edges, which empirically improves performance. Note that the orthogonalized kernel will be a sparse $s + 2k'$ kernel with values propagated from the original k size kernel. Since circular convolution is applied to the entire image, including the zero-padded regions of X_{pad}, these padded areas can acquire information from the central spatial region. As norm preservation only holds for $||X|| = ||X_{\text{pad}}|| = ||Y_{\text{pad}}||$, removing pixels from Y_{pad} will cause a slight norm drop. Importantly, it does not affect the validity of the certified results, as neither zero-padding nor the removal of padded parts expands the norm or violates the 1-Lipschitz bound.

For the BRONet architecture on ImageNet, we retain the padded regions in the output. Empirically, we found this beneficial, as it preserves more information from the feature map. We compensate for the resulting size increase by using a larger down-sampling stride in the neck module. For other datasets, we remove the padded regions to keep the input and output feature maps the same size. Further architectural implementation details are provided in Appendix B.

A.5. Complexity Comparison of Orthogonal Layers

In this section, we demonstrate the computational and memory advantages of the proposed method by analyzing its complexity compared to prior work. We use conventional notation from Prach et al. (2023). We focus on algorithmic complexity and required memory, particularly in terms of *multiply-accumulate operations (MACs)*. The detailed complexity comparison is presented in Table 8.

The analysis has two objectives: input transformation and parameter transformation. The computational complexity and memory requirements of the forward pass during training are the sum of the respective MACs and memory needs. The backward pass has the same complexity and memory requirements, increasing the overall complexity by a constant factor. In addition to theoretical complexity, we report the practical time and memory usage for different orthogonal layers under various settings in Figure 5 and Figure 6.

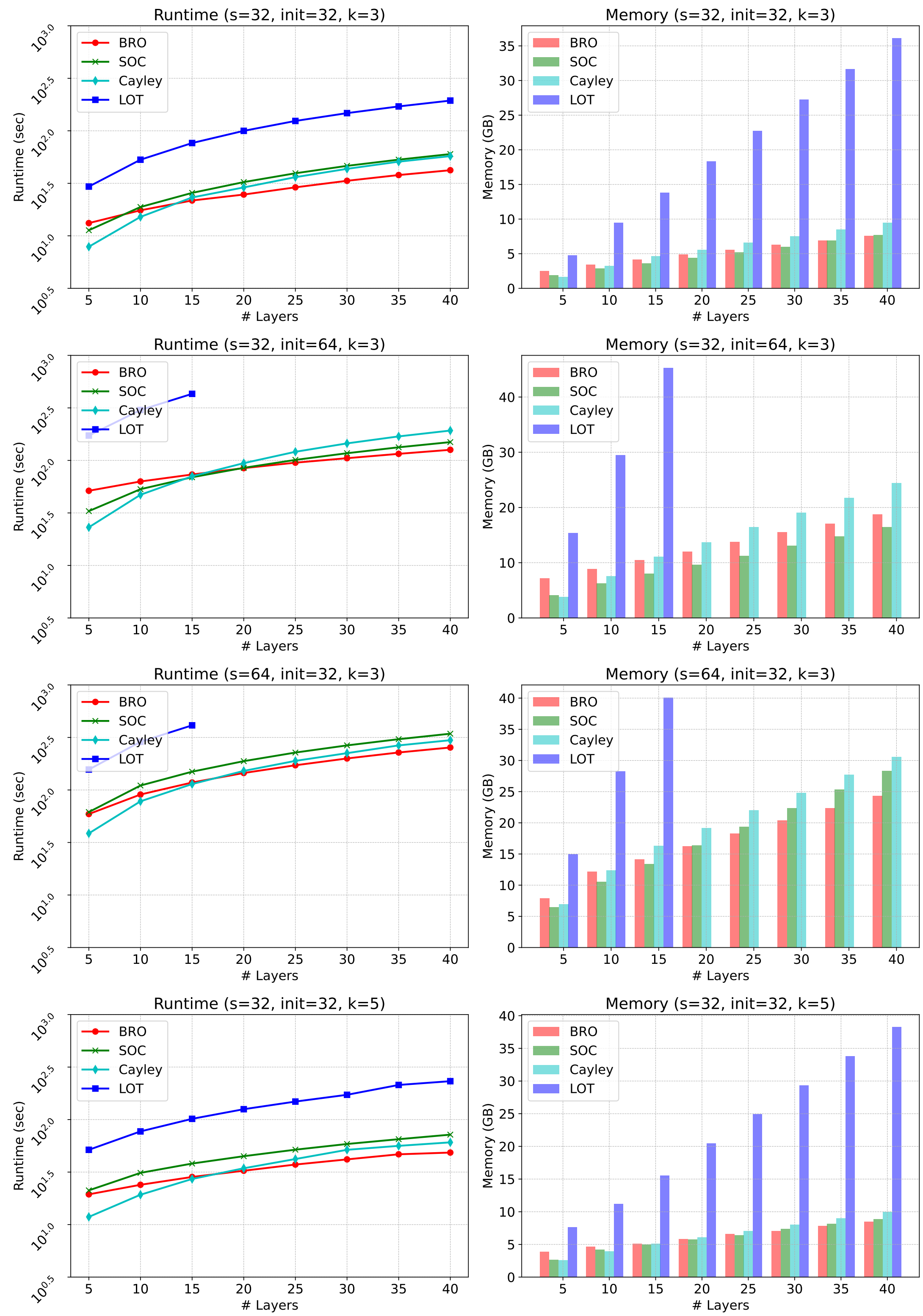

Figure 5. Demonstration of the runtime and memory consumption under different settings with LipConvNet architecture. The notation s denotes the input size, init denote the initial channel of the the entire model, and k denotes the kernel size. The batch sizes are fixed at 512 for all plots, and each value is the average over 10 iterations.

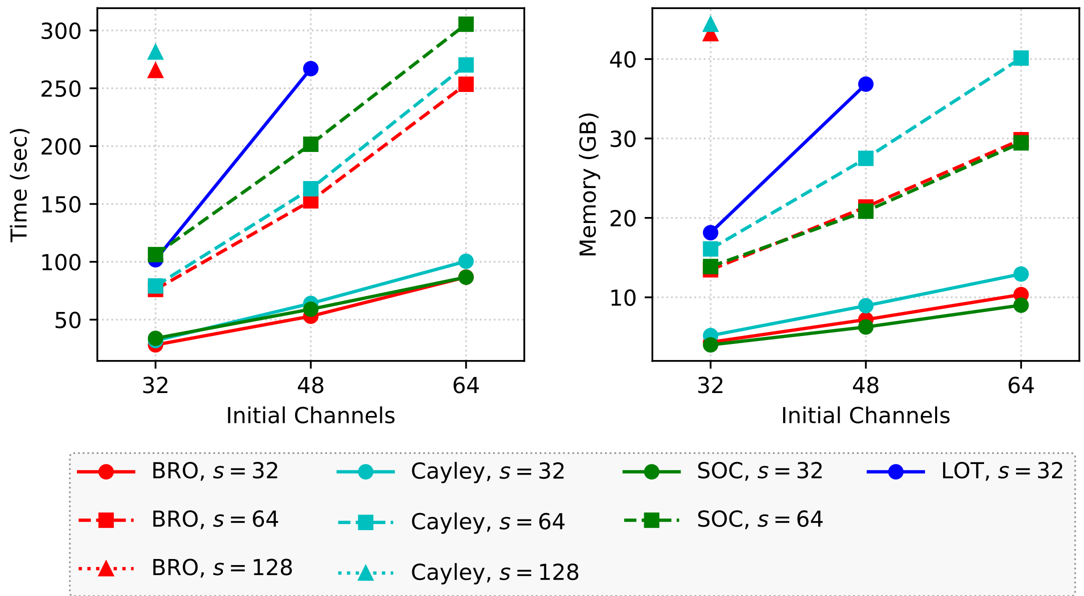

Figure 6. Demonstration of the runtime and memory consumption under different settings with LipConvNet architecture. For each line, we keep the input size s fixed while varying the initial channel. The batch sizes are fixed at 512 for all plots, and each value is the average over 10 iterations.

In the following analysis, we consider only dimension-preserving layers, where the input and output channels are equal, denoted by c. Define the input size as $s \times s \times c$, the batch size as b, the kernel size as $k \times k$, the number of inner iterations of a method as t, and the rank-control factor for BRO as κ, as listed in Table 7. To simplify the analysis, we assume $c > \log_2(s)$. Under the PyTorch (Paszke et al., 2019) framework, we can also assume that rescaling a tensor by a scalar and adding two tensors do not require extra memory during back-propagation.

Standard Convolution In standard convolutional layers, the computational complexity of the input transformation is $C = bs^2c^2k^2$ MACs, and the memory requirement for input and kernel are $M = bs^2c$ and $P = c^2k^2$, respectively. Additionally, these layers do not require any computation for parameter transformation.

SOC For the SOC layer, t convolution iterations are required. Thus, the input transformation requires computation complexity and memory t times that of standard convolution. For the parameter transformation, a kernel re-parameterization is needed to ensure the Jacobian of the induced convolution is skew-symmetric. During training, the SOC layer applies Fantastic Four (Singla & Feizi, 2021a) technique to bound the spectral norm of the convolution, which incurs a cost of c^2k^2t. The memory consumption remains the same as standard convolution.

LOT The LOT layer achieves orthogonal convolution via Fourier domain operations. Applying the Fast Fourier Transform (FFT) to inputs and weights has complexities of $\mathcal{O}(bcs^2\log(s^2))$ and $\mathcal{O}(c^2s^2\log(s^2))$, respectively. Subsequently, s^2 matrix orthogonalizations are required using the transformation $V(V^TV)^{-\frac{1}{2}}$. The Newton Method is employed to find the inverse square root. Specifically, let $Y_0 = V^TV$ and $Z_0 = I$, then Y_i is defined as

$$Y_{i+1} = \frac{1}{2}Y_i\left(3I - Z_iY_i\right), \quad Z_{i+1} = \frac{1}{2}\left(3I - Z_iY_i\right)Z_i. \tag{17}$$

This iteration converges to $(V^TV)^{-\frac{1}{2}}$. Executing this procedure involves computing $4s^2t$ matrix multiplications, requiring about $4s^2c^3t$ MACs and $4s^2c^2t$ memory. The final steps consist of performing $\frac{1}{2}bs^2$ matrix-vector products, requiring $\frac{1}{2}bs^2c^2$ MACs, as well as the inverse FFT. Given our assumption that $c > \log(s^2)$, the FFT operation is dominated by other operations. Considering the memory consumption, LOT requires padding the kernel from a size of $c \times c \times k \times k$ to $c \times c \times s \times s$, requiring bs^2c^2 memory. Additionally, we need to keep the outputs of the FFT and the matrix multiplications in memory, requiring about $4s^2c^2t$ memory each.

BRO Our proposed BRO layer also achieves orthogonal convolution via Fourier domain operations. Therefore, the input

Table 7. Notation used in this section.

Notation	Description
b	batch size
k	kernel size
c	input/output channels
s	input size (resolution)
t	number of internal iterations
κ	Rank-Control factor for BRO

Table 8. Computational complexity and memory requirements of different methods. We report multiply-accumulate operations (MACS) as well as memory requirements for batch size b, input size $s \times s \times c$, kernel size $k \times k$ and number of inner iterations t for SOC and LOT, rank-control factor $\kappa \in [0, 1]$ for BRO. We denote the complexity and memory requirement of standard convolution as $C = bs^2c^2k^2$, $M = bs^2c$, and $P = c^2k^2$, respectively.

Method	Input Transformations		Parameter Transformations	
	MACS $\mathcal{O}(\cdot)$	Memory	MACS $\mathcal{O}(\cdot)$	Memory $\mathcal{O}(\cdot)$
Standard	C	M	-	P
SOC	Ct	Mt	c^2k^2t	P
LOT	bs^2c^2	$3M$	$4s^2c^3t$	$4s^2c^2t$
Cayley	bs^2c^2	$2.5M$	s^2c^3	$1.5s^2c^2$
BRO	bs^2c^2	$2.5M$	$s^2c^3\kappa$	$2s^2c^2$

transformation requires the same computational complexity as LOT. However, by leveraging the symmetry properties of the Fourier transform of a real matrix, we reduce both the memory requirement and computational complexity by half. During the orthogonalization process, only $\frac{1}{2}s^2$ are addressed. The low-rank parameterization results in a complexity of approximately $s^2c^3\kappa$ and memory usage of $\frac{1}{2}s^2c^2$. Additionally, we need to keep the outputs of the FFT, the matrix inversion, and the two matrix multiplications in memory, requiring about $\frac{1}{2}s^2c^2t$ memory each.

Cayley Like BRO, the Cayley layer achieves orthogonal convolution in the Fourier domain and leverages real-matrix symmetry to reduce the input-transformation memory. Thus, its input-transformation complexity and memory match those of BRO. Its parameter-transformation, however, has complexity s^2c^3 with memory usage of $\frac{1}{2}s^2c^2$. Additionally, we need to keep the outputs of the FFT, the matrix inversion, and the single matrix multiplications in memory similarly demands about $\frac{1}{2}s^2c^2t$ each.

B. Implementation Details

In this section, we will detail our computational resources, the architectures of BRONet and LipConvNet, rank-n configuration, hyper-parameters used in LA loss, and experimental settings.

B.1. Computational Resources

Most of the experiments are conducted on a computer with an Intel Xeon Gold 6226R processor and 192 GB of DRAM memory. The GPU we used is the NVIDIA RTX A6000 (10,752 CUDA cores, 48 GB memory per card). For CIFAR-10 and CIFAR-100, we used a single A6000 card for training. For Tiny-ImageNet and diffusion data augmentation on CIFAR-10/100, we utilized distributed data parallel (DDP) across two A6000 cards for joint training. For the two ImageNet experiments in Table 1, they are conducted on an 8-GPU (NVIDIA H100) machine.

B.2. Architecture Details

The proposed BRO layer is illustrated in Figure 7. In this paper, we mainly use the BRO layer to construct two different architectures: BRONet and LipConvNet. We will first explain the details of BRONet, followed by an explanation of

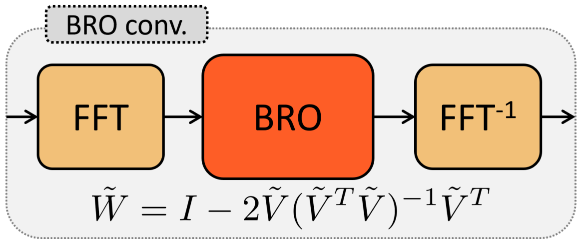

Figure 7. The proposed Block Reflector Orthogonal (BRO) convolution kernel, which is an orthogonal matrix, employs Fourier transformation to simulate the convolution operation. This convolution is inherently orthogonal and thus 1-Lipschitz, providing guarantees for adversarial robustness.

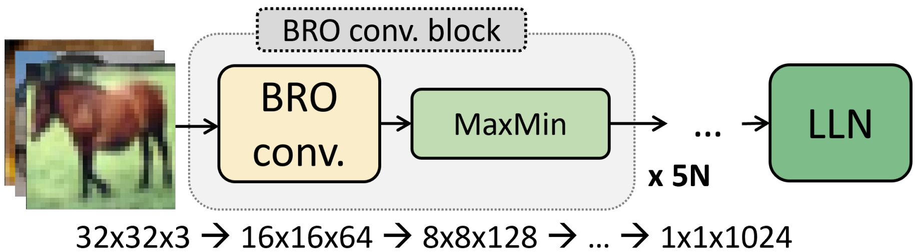

Figure 8. Following Trockman & Kolter (2021); Singla & Feizi (2021b); Xu et al. (2022), we use the proposed orthogonal convolution layer to construct the LipConvnet. This figure illustrates the LipConvnet-5, which cascades five BRO convolution layers. The activation function used is the MaxMin function, and the final layer is the last layer normalization (LLN).

LipConvNet constructed using the BRO layer.

BRONet Architecture We design our architecture BRONet similar to SLL and LiResNet. It consists of a stem layer for image-to-feature conversion, several convolutional backbone blocks of same channel width for feature extraction, a neck block for down-sampling and converting feature maps into flattened vectors, and multiple dense blocks followed by a spectral normalized layer (Singla et al., 2022). For non-linearity, MaxMin activation is used.

Compared to LiResNet with Lipschitz-regularized (Lip-reg) convolutional backbone blocks and SLL with SDP-based 1-Lipschitz layers, BRO orthogonal backbone blocks stabilize the gradient norm due to the property of orthogonal layers. We keep the first few layers (the first stem layer for all datasets and six extra layers for ImageNet) in BRONet to be Lipschitz-regularized since we empirically find it benefits the model training with a more flexible Lipschitz control in the early layers.

Figure 9 illustrates the details of the BRONet architecture, which is comprised of several key components:

- Stem: This consists of an unconstrained convolutional layer that is Lipschitz-regularized during training. The width W is the feature channel dimension, which is an adjustable parameter. For the ImageNet architecture, we extend the stem layer with six unconstrained Lipschitz-regularized convolution layers of same channel width, which we empirically found beneficial for feature extraction.
- Backbone: This segment consists of L BRO convolutional blocks with channel width W, each using $k = 3$ kernels and constrained to be 1-Lipschitz. Before applying BRO parameterization, we apply a fixed identity residual re-parameterization to the unconstrained parameter V: $V \leftarrow I + \frac{\alpha}{\sqrt{L}}V$, where I is the identity convolutional kernel and α is a learned scalar. This implementation is adapted from LiResNet (Hu et al., 2023; 2024), which was designed as a training trick for normalization-free networks. We also found it to be empirically effective in our setting.
- Neck: This consists of a convolutional down-sampling layer followed by a dense layer, which reduces the feature dimension. For the convolutional layer, we follow LiResNet (Hu et al., 2024) to construct a 1-Lipschitz matrix with dimension $(c_{\text{out}}, c_{\text{in}} \times k^2)$ and reshape it back to $(c_{\text{out}}, c_{\text{in}}, k, k)$. It is important to note that while the reshaped kernel

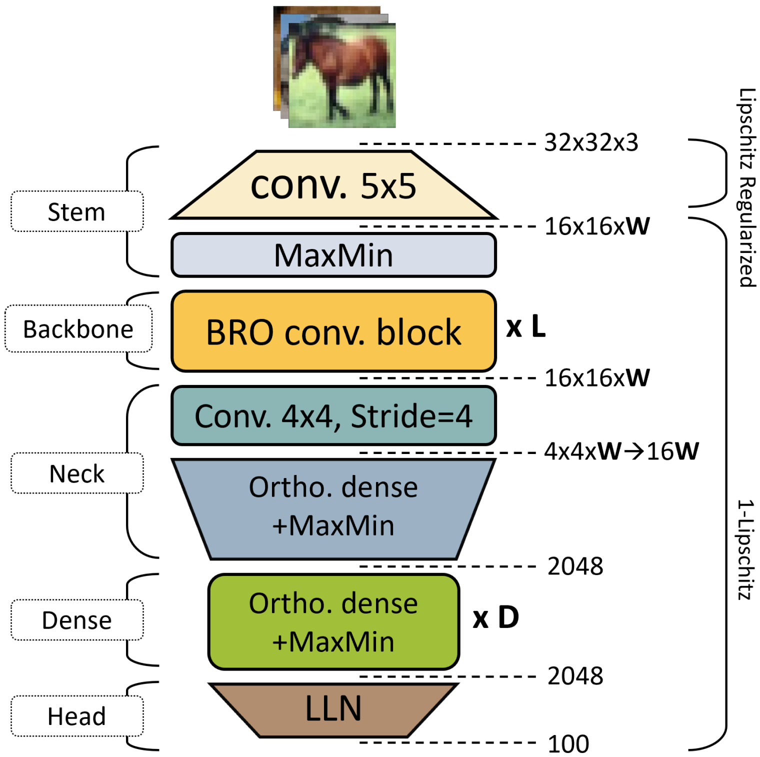

Figure 9. Following the LiResNet architecture (Leino et al., 2021; Hu et al., 2023), we utilized the BRO layer to construct **BRONet**. The parameters L, W, and D can be adjusted to control the model size.

differs from the orthogonal convolution described in BRO convolutional layer, it remains 1-Lipschitz bounded due to being non-overlapping (stride $=$ kernel size k) (Tsuzuku et al., 2018). For the ImageNet architecture, we replace the learnable convolution layer with ℓ_2-norm patch pooling, which is a norm-preserving nonlinear pooling layer that we found to work better on the ImageNet benchmark. Furthermore, as we do not remove the $2k'$ padded regions for the ImageNet zero-padding implementation (discussed in A.4), the output feature map size for each BRO convolutional layer increases. Consequently, we use a larger down-sampling stride to keep the feature map the same size before flattened.

- Dense: D BRO or Cholesky-orthogonal (Hu et al., 2024) dense layers with width 2048 are appended to increase the network's depth and enhance the model capability. The identity re-parameterization that is used in the backbone is also applied here with L replaced by D.
- Head: The architecture concludes with an LLN (Last Layer Normalization) layer, an affine layer that outputs the prediction logits.

We can use the W, L, and D to control the model size.

LipConvNet Architecture

This architecture is utilized in orthogonal neural networks such as SOC and LOT. The fundamental architecture, LipConvNet, consists of five orthogonal convolutional blocks, each serving as a down-sampling layer. The MaxMin or householder (Singla et al., 2022) activation function is employed for activation, and the final layer is an affine layer such as LLN. Figure 8 provides an illustration of LipConvNet. To increase the network depth, dimension-preserving orthogonal convolutional blocks are added subsequent to each down-sampling block; thus, the depth remains a multiple of five.

We use the notation LipConvNet-depth-width to describe the configurations. For example, LipConvNet-10-32 indicates a network with 10 convolutional layers and an initial channel width of 32, consisting of five downsampling semi-orthogonal layers and five dimension-preserving orthogonal layers.

B.3. Architecture and Rank-n Configuration

As mentioned in Section 4.1, for BRO layers with dimension $d_{\text{out}} = d_{\text{in}} = m$, we explicitly set the unconstrained parameter V to be of shape $m \times n$ with $m > n$ to avoid the degenerate case. An ablation study on the effect of different choices of rank-n is presented in Appendix D.3.

BRONet

We set $n = m/4$ for the BRONet-M backbone and dense layers on CIFAR-10/100 and set $n = m/8$ for the BRONet on Tiny-ImageNet. For all other BRONet experiments, we use $n = m/2$ for the BRO backbone and use Cholesky-orthogonal dense layers. For CIFAR-10/100, BRONet is configured with L12W512D8, and L6W512D4 for Tiny-ImageNet. For the ImageNet architecture, BRONet is configured with L14W588D8, with six Lipschitz-regularized layers and eight BRO convolutional layers. Specific architecture details are presented in Appendix B.2.

LipConvNet

For LipConvNet, we set $n = m/8$ for all experiments.

B.4. LA Hyper-parameters

Unless otherwise specified, the LA loss hyperparameters are set to $T = 0.75$, $\xi = 2$, and $\beta = 5.0$. For LipConvNet experiments, ξ is set to $2\sqrt{2}$. These hyperparameters were selected based on an ablation study conducted on LipConvNet. Please see Appendix D.5 for details.

B.5. Table 1 Details

Mainly following (Hu et al., 2024), we use NAdam (Dozat, 2016) and the LookAhead Wrapper (Zhang et al., 2019) with an initial learning rate of 10^{-3}, batch size of 256, and weight decay of 4×10^{-5}. The learning rate follows a cosine decay schedule with linear warm-up during the first 20 epochs, and the model is trained for a total of 800 epochs. We combine the LA loss with the EMMA (Hu et al., 2023) method to adjust non-ground-truth logit values for Lipschitz regularization on the stem layer. The target budget for EMMA is set to $\varepsilon = 108/255$ and offset for LA is set to $\xi = 2$. For ImageNet experiments, the batch size is set to 1024, with EMMA target budget $\varepsilon = 72/255$, and trained for a total of 400 epochs. Weight decay is removed for the ImageNet setting as we empirically found it hurt model performance. To report the results of LiResNet (Hu et al., 2024), we reproduce the results in the same setting without diffusion data augmentation for fair comparison. The experimental results are the average of three runs. For other baselines, results are reported as found in the literature.

B.6. Table 2 Details

In this table, we utilize diffusion-synthetic datasets pubicly available from (Hu et al., 2024; Wang et al., 2023) for CIFAR-10 and CIFAR-100, which contain 4 million and 1 million images, respectively. Following (Hu et al., 2024), we augment each 256 size minibatch with 1:3 real-to-synthetic ratio, resulting in a total batch size of 1024. We have removed weight decay, as we observed it does not contribute positively to performance with diffusion-synthetic datasets. For the ImageNet dataset, we generate 2 million images using the best setting recommended EDM2 with autoguidance Karras et al. (2024b;a), and use batch size 512 augmented with 1:1 real-to-synthetic ratio, resulting in a total batch size of 1024. All other settings remain consistent with those in Table 1.

B.7. Table 3 Details

The settings are consistent with those in Table 2, where we use the default architecture of LiResNet (L12W512D8), LA loss, and diffusion data augmentation. We replace the convolutional backbone for each Lipschitz layer.

B.8. Table 4 Details

Following the training configuration of Singla & Feizi (2021b), we adopt the SGD optimizer with an initial learning rate of 0.1, which is reduced by a factor of 0.1 at the 50-th and 150-th epochs, over a total of 200 epochs. Weight decay is set to 3×10^{-4}, and a batch size of 512 is used for the training process. The architecture is initialized with initial channel sizes of 32, 48, and 64 for different rows in the table. The LA loss is adopted for training.

C. Logit Annealing Loss Function

In this section, we delve into the details of the LA loss. Initially, we will prove Theorem 1, which illustrates the lower bound of the empirical margin loss risk. Next, we will visualize the LA loss and its gradient values. Additionally, we will discuss issues related to the CR term used in the SOC and LOT frameworks. Lastly, we will thoroughly explain the annealing mechanism.

C.1. Proof of Theorem 1

Here, we explain Theorem 1, which demonstrates how model capacity constrains the optimization of margin loss. The margin operation is defined as follows:

$$\mathcal{M}_f = f(x)_t - \max_{k \neq t} f(x)_k. \tag{18}$$

This operation is utilized to formulate margin loss, which is employed in various scenarios to enhance logit distance and predictive confidence. The margin loss can be effectively formulated using the *ramp loss* (Bartlett et al., 2017), which offers an analytic perspective on margin loss risk. The ramp loss provides a linear transition between full penalty and no penalty states. It is defined as follows:

$$\ell_{\tau,\text{ramp}}(f,x,y) = \begin{cases} 0 & \text{if } f(x)_t - \max_{k\neq t} f(x)_k \geq \tau, \\ 1 & \text{if } f(x)_t - \max_{k\neq t} f(x)_k \leq 0, \\ 1 - \frac{f(x)_t - \max_{k\neq t} f(x)_k}{\tau} & \text{otherwise.} \end{cases}$$

We employ the margin operation and the ramp loss to define margin loss risk as follows:

$$\mathcal{R}_\tau(f) := \mathbb{E}(\ell_{\tau,\text{ramp}}(\mathcal{M}(f(x),y))), \tag{19}$$

$$\hat{\mathcal{R}}_\tau(f) := \frac{1}{n}\sum_i \ell_{\tau,\text{ramp}}(\mathcal{M}(f(x_i),y_i)), \tag{20}$$

where $\hat{\mathcal{R}}_\tau(f)$ denotes the corresponding empirical margin loss risk. According to Mohri et al. (2018), a risk bound exists for this loss:

Lemma 4. *(Mohri et al., 2018, Theorem 3.3) Given a neural network f, let τ denote the ramp loss. Let $\mathcal{F}$ represent the function class of f, and let $\mathfrak{R}_S(.)$ denote the Rademacher complexity. Assume that S is a sample of size n. Then, with probability $1-\delta$, we have:*

$$\mathcal{R}_\tau(f) \leq \hat{\mathcal{R}}_\tau(f) + 2\mathfrak{R}_S(\mathcal{F}_\tau) + 3\sqrt{\frac{\ln(1/\delta)}{2n}}. \tag{21}$$

Next, apply the following properties for the prediction error probability:

$$\mathcal{P}_e = \Pr\left[\arg\max_i f(x)_i \neq y\right] = \Pr\left[-\mathcal{M}(f(x),y) \geq 0\right] \tag{22}$$

$$= \mathbb{E}\mathbf{1}\left[\mathcal{M}(f(x),y) \leq 0\right] \tag{23}$$

$$\leq \mathbb{E}(\ell_{\tau,\text{ramp}}(\mathcal{M}(f(x),y))) \tag{24}$$

$$= \mathcal{R}_\tau(f), \tag{25}$$

where $\mathcal{P}_e$ is the prediction error probability. Assuming that the $\mathcal{P}_e$ is fixed but unknown, we can utilize Lemma 4 and equation 25 to prove Theorem 1:

$$\hat{\mathcal{R}}_\tau(f) \geq \mathcal{P}_e - 2\mathfrak{R}_S(\mathcal{F}_\tau) - 3\sqrt{\frac{\ln(1/\delta)}{2n}}. \tag{26}$$

This suggests that the lower bound for the margin loss risk $\hat{\mathcal{R}}_\tau(f)$ may be influenced by the complexity of the model.

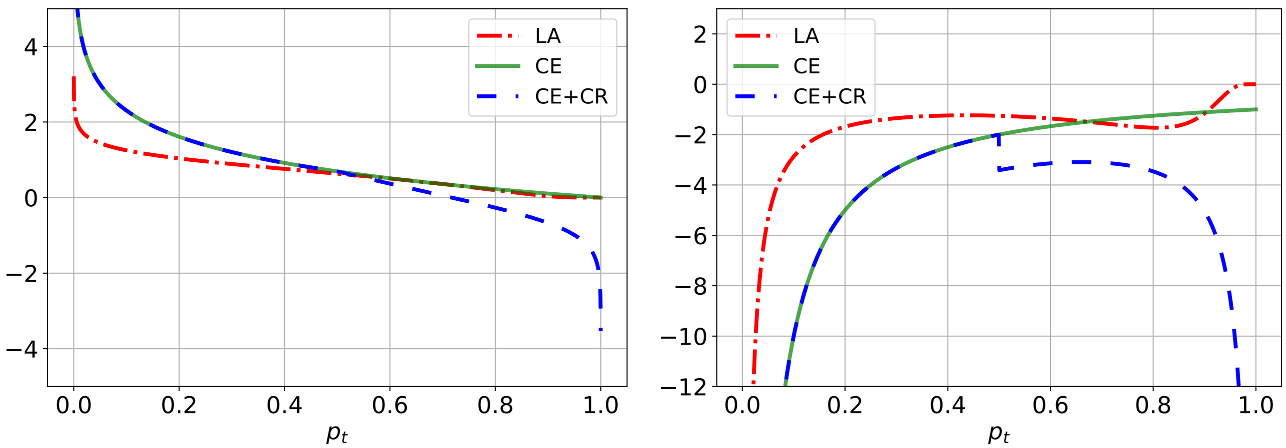

(a) Loss function (b) Derivative of loss function

Figure 10. Comparison of three loss functions. The x-axis is p_t. This figure displays curves representing the behavior of the proposed LA loss, contrasted with cross-entropy loss and the Certificate Regularization (CR) term. We observe the discontinuous gradient of the CR term. Additionally, the gradient of the CR term tends to infinity as p_t approaches one, leading to gradient domination and subsequently hindering the optimization of other data points. In contrast, the proposed LA loss employs a different strategy, where the gradient value anneals as nears one. This prevents overfitting and more effectively utilizes model capacity to enhance learning across all data points.

C.2. CR Loss Risk

Next, we illustrate and prove the relationship between margin loss risk and the CR loss risk. Let the empirical CR loss risk be defined as follows:

$$\hat{\mathcal{R}}_{CR}(f) := \frac{1}{n}\sum_i -\gamma \max(\mathcal{M}(f(x_i), y_i), 0). \tag{27}$$

Proposition 4. *Let $\hat{\mathcal{R}}_{CR}(f)$ and $\hat{\mathcal{R}}_\tau(f)$ be the empirical CR loss risk and margin loss risk, respectively. Assume that $\tau = \sup_i \mathcal{M}_f(x_i)$ and $\gamma = 1/\tau$. Then, $\hat{\mathcal{R}}_{CR}(f)$ is $\hat{\mathcal{R}}_\tau(f)$ decreased by one unit:*

$$\hat{\mathcal{R}}_{CR}(f) = \hat{\mathcal{R}}_\tau(f) - 1. \tag{28}$$

Proof. (Proof for Proposition 4) Consider two cases based on the value of $\mathcal{M}(x)$:

- When $\mathcal{M}(x) \le 0$: the CR loss is always zero and the ramp loss is always one. Thus, the distance between $\hat{\mathcal{R}}_{CR}(f)$ and $\hat{\mathcal{R}}_\tau(f)$ is one.
- When $\mathcal{M}(x) > 0$: The distance between the ramp loss and CR loss is:

$$\begin{aligned}\ell_{\tau,\text{ramp}}(\mathcal{M}(f(x_i), y_i)) + \gamma \max(\mathcal{M}(f(x_i), y_i), 0) &= 1 - \frac{\mathcal{M}(x_i)}{\tau} + \gamma\mathcal{M}(x_i) \\ &= 1 + (\gamma - \frac{1}{\tau})\mathcal{M}(x_i).\end{aligned} \tag{29}$$

Therefore, the empirical CR loss risk can be rewritten as:

$$\hat{\mathcal{R}}_{CR}(f) = \hat{\mathcal{R}}_\tau(f) - 1 - (\gamma - \frac{1}{\tau})M_+, \text{ where} \tag{30}$$

$$M_+ = \sum\nolimits_{x_i \in \{x_i | \mathcal{M}(x_i) > 0\}} \mathcal{M}(x_i). \tag{31}$$

This equation simplifies to the one stated in Proposition 4 if $\gamma = 1/\tau$. □

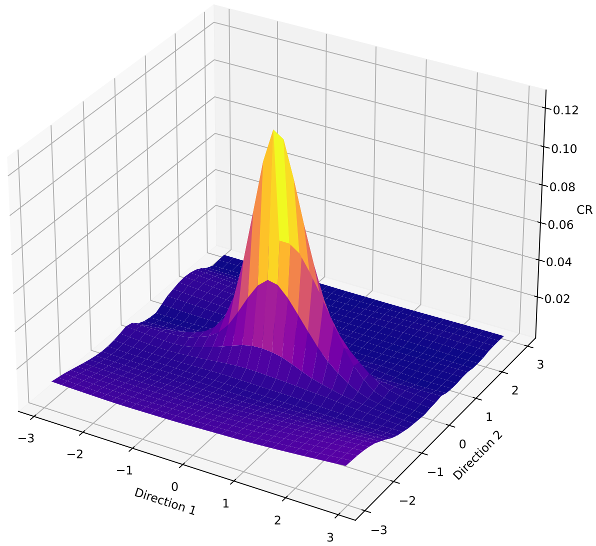

(a) CR landscape

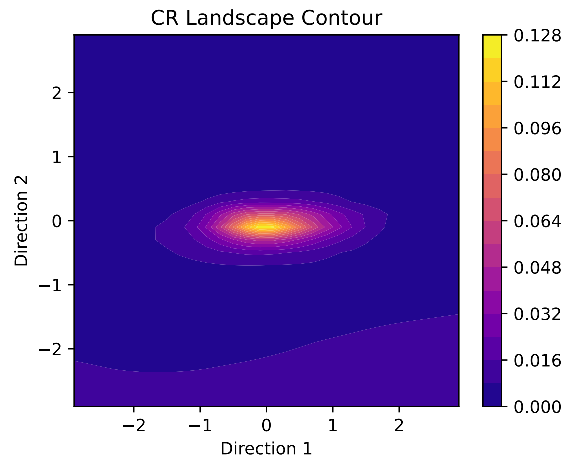

(b) CR landscape contour plot

Figure 11. CR Loss Landscape Analysis. This figure illustrates the loss landscape to investigate the effects of the CR term. Notably, the CR term can suddenly become "activated" or "deactivated," which is vividly depicted in the landscape transitions. These abrupt changes contribute to unstable optimization during training, potentially affecting the convergence and reliability of the model. Understanding this behavior is crucial for improving the training process of Lipschitz neural networks. Regarding the direction of loss landscape, we follow the setting in Engstrom et al. (2018) and Chen et al. (2021). We visualize the loss landscape function $z = \mathcal{L}_{CR}(x, w + \omega_1 d_1 + \omega_2 d_2)$, where $d_1 = sign(\nabla_w \mathcal{L}_{CR})$, $d_2 \sim Rademacher(0.5)$, and ω is the grid.

Conclusively, we demonstrate that the CR loss risk has a lower bound as follows:

$$\hat{\mathcal{R}}_{CR}(f) \geq \mathcal{P}_e - 2\mathfrak{R}_S(\mathcal{F}_\tau) - 3\sqrt{\frac{\ln(1/\delta)}{2n}} - 1. \quad (32)$$

When the complexity is limited, CR loss risk may exhibit a great lower bound. Thus, enlarging margins using the CR term is less beneficial beyond a certain point.

C.3. CR Issues

Recall that CE loss with CR term is formulated as: $\mathcal{L}_{\mathrm{CE}} - \gamma \max(\mathcal{M}_f(x), 0)$, where $\mathcal{M}_f(x) = f(x)_t - \max_{k \neq t} f(x)_k$ is the logit margin between the ground-truth class t and the runner-up class. We compare LA loss, CE loss, and the CE+CR loss with $\gamma = 0.5$. Figure 10 illustrates the loss values and their gradient values with respect to p_t, where p_t represents the softmax result of the target logit. When using CR term as the regularization for training Lipschitz models, we summarize the following issues:

(1). Discontinuous loss gradient: the gradient value of CR term at $p_t = 0.5$ is discontinuous This discontinuity leads to unstable optimization processes, as shown in Figure 10. This indicates that, during training, the CR loss term may be "activated" or "deactivated." This phenomenon can be further explored through the loss landscape. Figure 11 displays the CR loss landscape for the CR term, where it can be seen that the CR term is activated suddenly. The transition is notably sharp.

(2). Gradient domination: as p_t approaches one, the gradient value escalates towards negative infinity. This would temper the optimization of the other data points in the same batch.

(3). Imbalance issue: our observations indicate that the model tends to trade clean accuracy for increased margin, suggesting a possible imbalance in performance metrics.

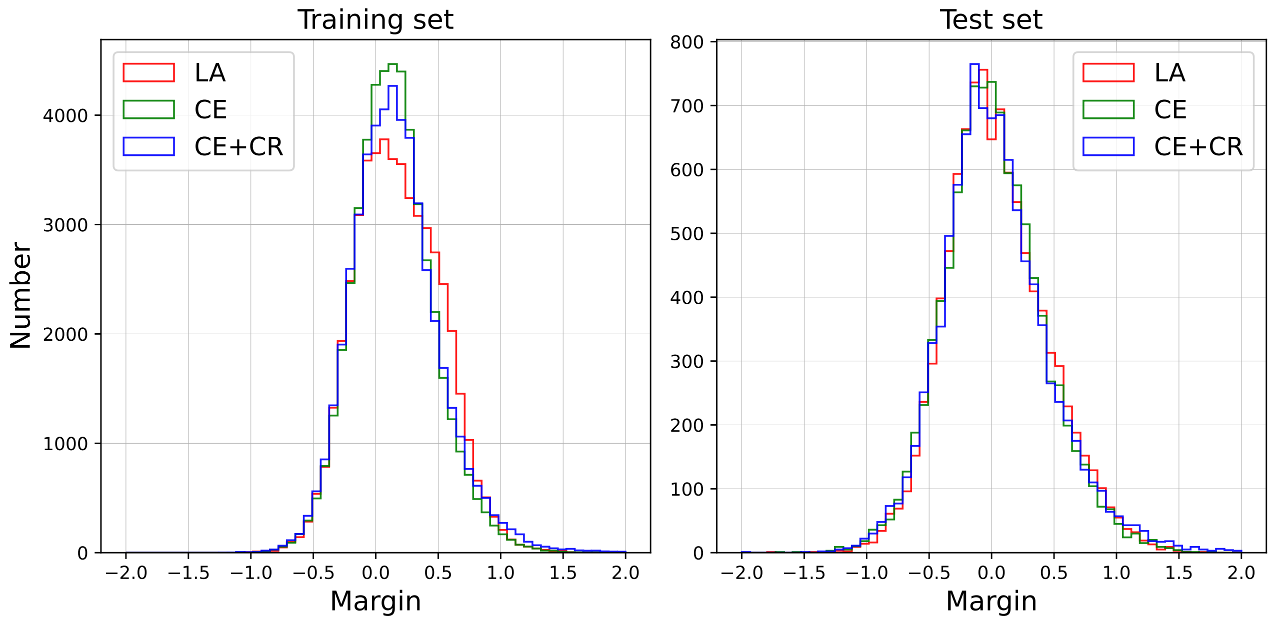

Figure 12. Histogram of margin distribution. The left histogram represents margin distribution obtained from the training set, while the right histogram shows margin distribution from the test set. The x-axis represents the margin values. These visualizations demonstrate that the LA loss helps the model learn better margins.

Table 9. Additional results on Tiny-ImageNet. No additional diffusion-generated synthetic datasets are used during training.

Datasets	**Models**	**#Param.**	**Clean Acc.**	**Certified Acc. (ε)**		
				$\frac{36}{255}$	$\frac{72}{255}$	$\frac{108}{255}$
Tiny-ImageNet	SLL X-Large (Araujo et al., 2023)	1.1B	32.1	23.2	16.8	12.0
	Sandwich (Wang & Manchester, 2023)	39M	33.4	24.7	18.1	**13.4**
	LiResNet† (Hu et al., 2024)	133M	40.9	26.2	15.7	8.9
	BRONet	75M	40.5	26.9	17.1	10.1
	BRONet (+LA)	75M	**41.2**	**29.0**	**19.0**	12.1

Therefore, instead of using the CR term to train Lipschitz neural networks, we design the LA loss to help Lipschitz models learn better margin values.

C.4. Annealing Mechanism

We can observe the annealing mechanism in the right subplot of Figure 10. The green curve is the gradient value of the LA loss. We can observe that the gradient value is gradually annealed to zero as the p_t value approaches one. This mechanism limits the optimization of the large-margin data points. As mentioned previously, Lipschitz neural networks have limited capacity, so we cannot maximize the margin indefinitely. Since further enlarging the margin for data points with sufficiently large margin is less beneficial, we employ the annealing mechanism to allocate the limited capacity for the other data points.

In addition, we delve deeper into the annealing mechanism of the proposed LA loss function. As illustrated in Figure 12, we train three different models using three loss functions, and we plot the histogram of their margin distribution. The red curve represents the proposed LA loss. Compared to CE loss, the proposed LA loss has more data points with margins between 0.4 and 0.8. This indicates that the annealing mechanism successfully improves the small-margin data points to appropriate margin 0.4 and 0.8.

Additionally, as the left subplot in Figure 12 illustrates, the margin exhibits an upper bound; no data points exceed a value of

Table 10. The clean, certified, and empirical robust accuracy of BRONet-M on CIFAR-10, CIFAR-100, and Tiny-ImageNet.

Datasets	Clean Acc.	Certified / AutoAttack (ε)		
		$\frac{36}{255}$	$\frac{72}{255}$	$\frac{108}{255}$
CIFAR-10	81.1	69.9 / 76.1	55.3 / 69.7	40.4 / 62.6
CIFAR-100	54.3	40.0 / 47.3	28.7 / 41.0	19.4 / 35.5
Tiny-ImageNet	41.0	29.2 / 36.3	19.7 / 31.7	12.3 / 27.5

2.0, even when a larger γ is used in the CR term.

This observation coincides with our theoretical analysis, confirming that the Lipschitz models cannot learn large margins due to its limited capacity.

Table 11. The clean accuracy, empirical accuracy against ℓ_∞ adversary, and certified accuracy on CIFAR-10.

Methods	Clean	$\ell_\infty = 2/255$	$\ell_\infty = 8/255$	Certified Acc.
STAPS	79.8	65.9	N/A	62.7 ($\ell_\infty = 2/255$)
SABR	79.5	65.8	N/A	62.6 ($\ell_\infty = 2/255$)
IBP	48.9	N/A	35.4	35.3 ($\ell_\infty = 8/255$)
TAPS	49.1	N/A	34.8	34.6 ($\ell_\infty = 8/255$)
SABR	52.0	N/A	**35.7**	35.3 ($\ell_\infty = 8/255$)
BRONet-L	**81.6**	**68.8**	21.0	70.6 ($\ell_2 = 36/255$) 57.2 ($\ell_2 = 72/255$) 42.5 ($\ell_2 = 108/255$)

D. Additional Experiments

In this section, we present additional experiments and ablation studies.

D.1. Additional Tiny-ImageNet Results for Table 1

We present additional results on the Tiny-ImageNet dataset in Table 9. The model configuration is described in Appendix B.3 and the training setting is consistent with CIFAR-10/100 in Table 1.

D.2. Empirical Robustness

In addition to certified robustness, we can validate the empirical robustness of the proposed method. This further supports our robustness certificate. Theoretically, certified robust accuracy is the lower bound for the worst-case accuracy, while empirical robust accuracy is the upper bound for the worst-case accuracy. Thus, empirical robust accuracy must be greater than certified robust accuracy. We employ AutoAttack (Croce & Hein, 2020) to assess empirical robustness. The certified and empirical robust accuracy for different attack budgets are illustrated in Table 10. We observe that all empirical robust accuracy values for each budget are indeed higher than their corresponding certified accuracy. This indicates that the certification is correct under the AutoAttack, and that the proposed method achieves strong empirical robustness without any expensive adversarial training examples. Furthermore, we also measure ℓ_∞ empirical robustness against ℓ_∞ AutoAttack on CIFAR-10. The results are presented in Table 11, and the baselines for ℓ_∞ certified defenses are from the literature (Mueller et al., 2023; Mao et al., 2023). Although not designed for ℓ_∞ certified robustness, our method shows competitive performance on the benchmark.

D.3. BRO Rank-n Ablation Experiments

As mentioned earlier, we can control the rank of V to construct the orthogonal weight matrix. In this paper, the matrix V is of low rank. Considering the internal term $V(V^TV)^{-1}V^T$ in our method's parameterization, the concept is similar to that of

Table 12. We compare the clean accuracy, certified accuracy, and training time for different choices of n for the unconstrained parameter V on CIFAR-100 with BRONet L6W256D4 and L6W512D4. Time is calculated in minutes per training epoch.

n	**L6W256D4**					**L6W512D4**				
	Clean	$\frac{36}{255}$	$\frac{72}{255}$	$\frac{108}{255}$	**Time**	**Clean**	$\frac{36}{255}$	$\frac{72}{255}$	$\frac{108}{255}$	**Time**
$m/8$	51.6	39.2	28.3	19.5	0.66	52.8	40.2	28.6	20.3	1.57
$m/4$	52.8	39.5	27.9	19.7	0.73	54.0	40.2	28.3	19.3	1.92
$m/2$	53.4	39.0	27.3	18.5	0.94	54.1	39.7	27.7	18.6	2.82
$3m/4$	52.7	39.5	28.0	19.2	1.27	53.5	39.8	27.9	18.9	3.75

Table 13. The improvement of LA loss with LipConvNet-10-32 on different datasets.

Datasets	**Loss**	**Clean**	$\frac{36}{255}$	$\frac{72}{255}$	$\frac{108}{255}$
CIFAR-10	CE	77.5	62.1	44.8	29.2
	LA	76.9	63.4	47.2	32.6
CIFAR-100	CE	48.5	34.1	22.6	14.4
	LA	48.6	35.4	24.5	16.1
Tiny-ImageNet	CE	38.0	26.3	17.0	10.3
	LA	39.4	28.1	18.2	11.6

LoRA (Hu et al., 2022). We further investigate the effect of different n values of V. For the unconstrained $m \times n$ parameter V in the backbone and dense blocks of BRONet, we conduct experiments using different n values. The clean and certified accuracy, as well as training time, on CIFAR-100 are presented in Table 12. Different values of n result in slight variations in performance, with $n = m/2$ yielding the best results. Therefore, we choose $n = m/4$ for all CIFAR-10/CIFAR-100 experiments on BRONet-M, and $n = m/2$ for BRONet-L and ImageNet. For Tiny-ImageNet, we set $n = m/8$ to mitigate overfitting.

D.4. LA Loss Ablation Experiments

We verify the LA loss on LipConvNet constructed using BRO, LOT, or SOC. Table 15 illustrates the improvement achieved by replacing the CE+CR loss, which is initially recommended for training LipConvNet. The results suggest that using the LA loss improves the performance of LipConvNet constructed with all orthogonal layers on both CIFAR-100 and Tiny-ImageNet.

We also compare LA to CE on LipConvNet. Table 13 shows the results for LipConvNet constructed with BRO. Our results show that the LA loss encourages a moderate margin without compromising clean accuracy. Notably, the LA loss is more effective on larger-scale datasets, suggesting that the LA loss effectively addresses the challenge of models with limited Rademacher complexity.

D.5. LA Loss Hyper-parameters Experiments

There are three tunable parameters in LA loss: temperature T, offset ξ, and annealing factor β. The first two parameters control the trade-off between accuracy and robustness, while the last one determines the strength of the annealing mechanism. For the temperature and offset, we slightly adjust the values used in Prach & Lampert (2022) to find a better trade-off position, given the differences between their network settings and ours. Specifically, we evaluated the temperature $T \in \{0.25, 0.5, 0, 75, 1.0\}$, the offset $\xi \in \{0.5, 1.0, 1.5, 2.0, 2.5, 3.0\}$, and the annealing factor $\beta \in \{1, 3, 5, 7\}$ with LipConvNet-10-32 on CIFAR-100. Based on the evaluation, all other LA experiments are set with $T = 0.75, \xi = 2.0$, and $\beta = 5.0$. For further LipConvNet experiments, the offset is set to $\xi = 2\sqrt{2}$ due to an oversight in the implementation. As we have found these hyper-parameters to work well, we did not further finetune them for each architecture and datasets to save computational cost. One might consider further refine the hyper-parameters for better performance. Additionally, we present the results of LA loss with different β values for LipConvNet-10 on CIFAR-100 in Table 14.

Table 14. Experimental results for LipConvNet-10 on CIFAR-100 for different values of β in the LA loss.

β **value**	**Clean**	$\frac{36}{255}$	$\frac{72}{255}$	$\frac{108}{255}$
1	48.63	35.48	24.36	17.19
3	48.57	35.68	24.78	16.66
5	49.09	35.58	24.46	16.38
7	49.02	35.72	24.34	16.05

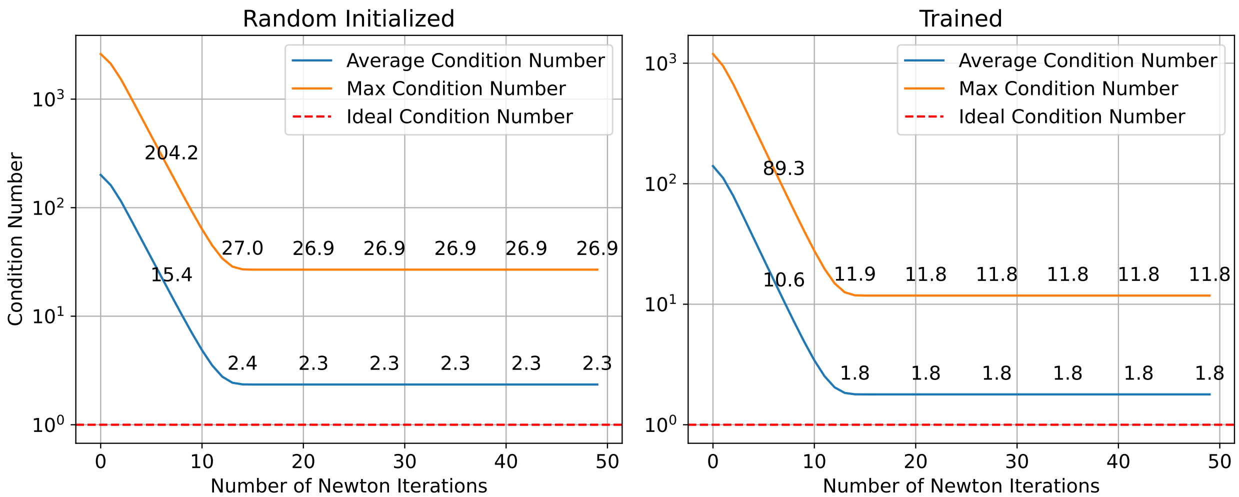

Figure 13. Plots of condition number of parameterized matrix in Fourier domain. The left plot shows the condition number with randomly initialized parameters, whereas the right plot shows the condition number with trained parameters.

D.6. LipConvNet Ablation Experiments

More detailed comparison stem from Table 4 are provided in Table 15, demonstrating the efficacy of LA loss across different model architectures and orthogonal layers. Following the same configuration as in Table 4, we further investigate the construction of LipConvNet by conducting experiments with varing initial channels and model depths, as detailed in Table 16.

D.7. Instability of LOT Parameterization

During the construction of the LOT layer, we empirically observed that replacing the identity initialization with the common Kaiming initialization for dimension-preserving layers causes the Newton method to converge to a non-orthogonal matrix. We check orthogonality by computing the condition number of the parameterized matrix of LOT in the Fourier domain. For an orthogonal layer, the condition number should be close to one. However, even after five times the iterations suggested by the authors, the result for LOT does not converge to one. Figure 13 illustrates that, even with 50 iterations, the condition number of LOT does not converge to one. The orange curve represents the case with Kaiming randomly initialized parameters, while the blue curve curve corresponds to the case after a few training epochs. Both exhibit a significant gap compared to the ideal case, indicating that LOT may produce a non-orthogonal layer.

Table 15. Comparison of clean and certified accuracy, training and inference time (seconds/epoch), and number of parameters with different orthogonal layers in LipConvNet-10. Instances marked with a dash (-) indicate out of memory during training. In the Time column, we show the training time, and the inference time is in brackets. Time is calculated in minutes per training epoch.

Init. Width	Methods	CIFAR-100					Tiny-ImageNet				
		Clean	$\frac{36}{255}$	$\frac{72}{255}$	$\frac{108}{255}$	**Time**	**Clean**	$\frac{36}{255}$	$\frac{72}{255}$	$\frac{108}{255}$	**Time**
32	SOC + CR	48.1	34.3	23.5	15.6	19.2	37.4	26.2	17.3	11.2	107.7
	LA	47.5	34.7	24.0	15.9	(5.3)	38.0	26.5	17.7	11.3	(11.1)
	LOT + CR	48.8	34.8	23.6	15.8	52.7	38.7	26.8	17.4	11.3	291.5
	LA	49.1	35.5	24.4	16.3	(1.4)	40.2	27.9	18.7	11.8	(7.3)
	BRO + CR	48.4	34.7	23.6	15.4	17.3	38.5	27.1	17.8	11.7	98.6
	LA	48.6	35.4	24.5	16.1	(0.9)	39.4	28.1	18.2	11.6	(4.6)
48	SOC + CR	48.4	34.9	23.7	15.9	35.4	38.2	26.6	17.3	11.0	199.3
	LA	48.2	34.9	24.4	16.2	(8.7)	38.9	27.1	17.6	11.2	(20.3)
	LOT + CR	49.3	35.3	24.2	16.3	143.0	-	-	-	-	-
	LA	49.4	35.8	24.8	16.3	(3.0)	-	-	-	-	
	BRO + CR	49.4	35.7	24.5	16.3	35.2	38.9	27.2	18.0	11.6	196.9
	LA	49.4	36.2	24.9	16.7	(1.1)	40.0	28.1	18.9	12.3	(4.8)
64	SOC + CR	48.4	34.8	24.1	16.0	53.1	38.6	26.9	17.3	11.0	305.1
	LA	48.5	35.5	24.4	16.3	(12.4)	39.3	27.3	17.6	11.2	(32.5)
	LOT + CR	49.4	35.4	24.4	16.3	301.8	-	-	-	-	-
	LA	49.6	36.1	24.7	16.2	(5.8)	-	-	-	-	
	BRO + CR	49.7	35.6	24.5	16.4	64.4	39.6	27.9	18.2	11.9	355.3
	LA	49.7	36.7	25.2	16.8	(1.6)	40.7	28.4	19.2	12.5	(4.9)

Table 16. The experiments conducted with varying initial widths and model depths using the CIFAR-100 and Tiny-ImageNet datasets. The model employed is LipConvNet.

Depth	Init. Width	CIFAR-100				Tiny-ImageNet			
		Clean	$\frac{36}{255}$	$\frac{72}{255}$	$\frac{108}{255}$	**Clean**	$\frac{36}{255}$	$\frac{72}{255}$	$\frac{108}{255}$
5	32	49.04	35.06	24.19	16.06	39.28	27.47	18.23	11.47
	48	49.60	35.80	24.63	16.20	40.12	27.79	18.36	11.92
	64	49.97	36.21	24.92	16.45	40.82	28.26	18.76	12.31
10	32	48.62	35.36	24.48	16.11	39.37	28.06	18.16	11.58
	48	49.39	36.19	24.86	16.68	39.98	28.12	18.86	12.27
	64	49.74	36.70	25.24	16.80	40.66	28.36	19.24	12.48
15	32	48.59	35.51	24.42	16.28	39.20	27.66	18.08	11.84
	48	49.37	36.50	24.93	16.81	39.87	27.96	18.49	12.11
	64	49.91	36.57	25.26	16.81	40.38	28.73	18.78	12.52
20	32	48.62	35.68	24.66	16.57	38.74	27.23	17.75	11.67
	48	49.26	36.09	24.91	16.62	39.63	27.88	18.49	12.07
	64	49.60	36.47	25.24	17.09	39.77	28.03	18.53	12.17

E. Limitations

While our proposed methods have demonstrated improvements across several metrics, the results for large perturbations, such as $\varepsilon = 108/255$, are less consistent. Additionally, the proposed LA loss requires extra hyperparameter tuning. In our experiments, the parameters were chosen based on LipConvNets trained on CIFAR-100 without diffusion-synthetic augmentation (Appendix B.4), which may not fully align with different models and datasets. Furthermore, our methods are specifically designed for ℓ_2 certified robustness, and certifying against attacks like ℓ_∞-norm introduces additional looseness. Lastly, although BRO addresses some limitations of orthogonal layers, training certifiably robust models on large datasets remains computationally expensive.